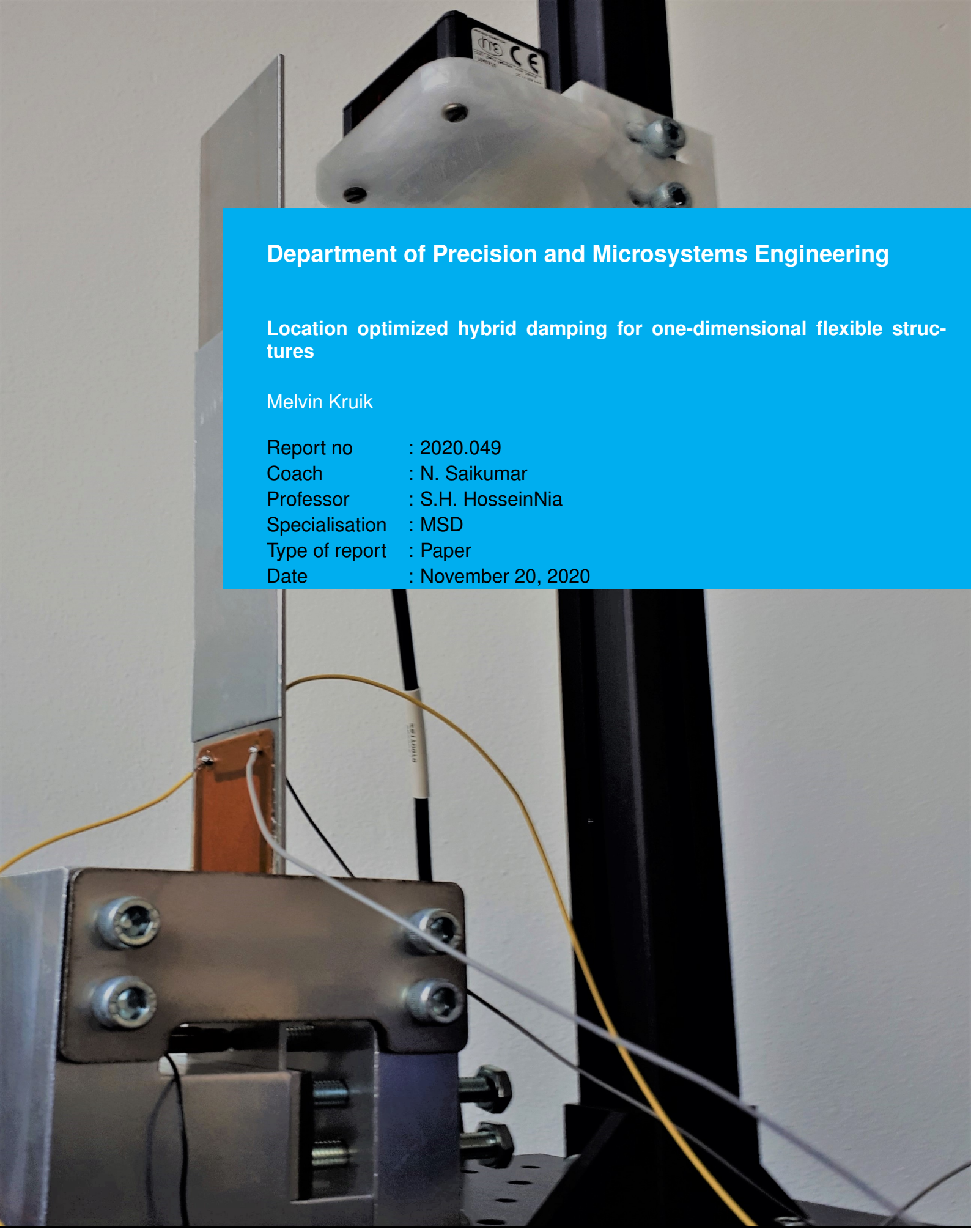

## Department of Precision and Microsystems Engineering

# Location optimized hybrid damping for one-dimensional flexible structures

Melvin Kruik

Report no : 2020.049
Coach : N. Saikumar
Professor : S.H. HosseinNia
Specialisation : MSD
Type of report : Paper
Date : November 20, 2020

TU Delft Delft University of Technology

Challenge the future

# Location optimized hybrid damping for one-dimensional flexible structures

*M. Kruik, S.H. HosseinNia, N. Saikumar*

## Abstract

Damping vibrations of flexible structures is a subject of importance in several industries, as the aerospace and high-tech industry. Especially when the ratio of damping over weight needs to be high. In literature optimization of this ratio is achieved in several manners, through optimization of individual damping methods, ie. active and passive damping. And through combining those methods to have passive damping supporting active damping. This paper introduces a novel hybrid damping method, which achieves further optimization of the ratio. This is done through analyses of the eigenmodes of the flexible structure and the properties of the damping methods, to find the optimal damping method for each eigenfrequency individually. Later on those methods are combined in the hybrid damping method, to ensure damping of a wide bandwidth of eigenfrequencies. This all is obtained by researching the properties of the individual damping methods, constrained layer damping (CLD) and active damping (AD), and the influence of combining those in a hybrid system. With this knowledge a methodology to optimize hybrid damping for a generic one-dimensional structure is developed, including rules-of-thumb aimed at simplifying the optimization approach.

---

## Nomenclature

| | |
|---|---|
| $\eta_{CLD,piezo}$ | Loss factor CLD and active damping(AD), respectively |
| $\eta_{exp}$ | Experimental loss factor system |
| $\eta_{num}$ | Numerical loss factor system |
| $\eta_{system}$ | Loss factor system |
| $\omega_c$ | Cut-off frequency controller |
| $\overline{u}$ | Displacement vector all nodes |
| $\overline{u}_{sensor}$ | Displacement vector sensor nodes |
| $\phi_{system}$ | Strain energy ratio |
| $\xi_{damp}$ | Damping factor controller |
| $a$ | Amplitude of vibration |
| $a_{opt}$ | Amplitude of vibration with optimized transducers |
| $F_{act}$ | Force vector generated by actuator |
| $F_{disturbance}$ | Disturbance force vector |
| $G_v$ | Shear modulus viscoelastic material |
| $G_v^n$ | Shear modulus viscoelastic material, $n^{th}$ eigenfrequency |
| $h_p^n$ | Thickness piezo transducer/layer, $n^{th}$ eigenfrequency |
| $h_{c,v}$ | Thickness contraining and viscoelastic layer, respectively |
| $H_{controller}$ | Transfer function PPF |
| $L_{patch}^n$ | Length of damping patch, $n^{th}$ eigenfrequency |
| $L_{peak}$ | Length of strain energy peak |
| $m_{patch}$ | Weight of damping patch |
| $U_b$ | Strain energy beam |
| $U_c$ | Strain energy constraining layer |
| $U_p$ | Strain energy piezo layer |
| $U_v$ | Strain energy viscoelastic layer |
| $U_{damped}$ | Strain energy dissipated per cycle |
| $U_{system}$ | Strain energy stored per cycle, beam and damping layers together |
| $V_{act}$ | Voltage actuator |
| $V_{act}^{max}$ | Maximum allowable voltage transducers |
| $V_{sen}$ | Voltage sensor |

| | | | | | |
|---|---|---|---|---|---|
| $w_{tip}^{damped}$ | Lateral tip displacement, damped case | g | Controller gain | x | Location on beam, value between 0 and dL |
| | | i | Loop count | | |
| dL | Length of a FE-element | n | Eigenfrequency indicator | Y(s) | Transfer function, $\frac{w_{tip}}{F_{disturbance}}$ |

## 1 Introduction

Damping out vibrations is a subject of increasing importance, since damping will increase dynamic performance of a structure, through reducing the amplitudes of eigenfrequencies. While, on the other hand, the mass of the object needs to stay as low as possible, since weight reduction reduces the amount of energy needed to influence dynamics. For this combination of reasons the subject of low weight flexible structures with additional damping will be elaborated in this paper.

In the aerospace industry this approach is applied in for example aeroplane wings. In those structures weight reduction increases efficiency and damping improves lifetimes. Those goals are achieved by using passive damping mainly, such as constrained layer damping (CLD). This damping method has as benefit the property to dampen out a certain energy percentage [19]. Consequently the same damping performance can be achieved for small and large amplitude vibrations. CLD has as downside the property to have damping capabilities dependent on frequency and temperature, this increases the difficulty of selecting the most suitable material [26]. In the high-tech industry the approach of low mass with additional damping is used to obtain high accuracy at high accelerations. This is for example useful in fast and accurate robot-arms, to reduce deformations of flexures. In this industry active damping (AD) is a popular method, because it can achieve high effectiveness, from a damping to weight ratio perspective. However, electronic hardware properties can reduce performance, due to the occurrence of low-pass filtering properties [29]. This active method does dampen out a certain energy percentage, like CLD. However saturation of the actuator will limit performance. Consequently damping performance is among others a function of the amplitude of the vibration.

As seen, different industries use different damping methods to influence dynamic performance, since each individual method offers case-specific benefits. In literature extensive research is done on optimization of those methods. For CLD those optimisations are done on the locations and dimensions of damping patches [9, 5]. In those researches the optimizations are carried out in a numerical manner. Those approaches lead to optimal damping patches, however those do not give insight in the properties of influence. Active damping of flexures can be done with different types of active elements [34, 25, 18]. The method used in this research is adding elongating piezo transducers onto the structure, figure 7 [25]. Since this method provides a collocated system [25] and because the stresses generated by the actuator do counteract the bending stresses in the structure. The stresses are visualized in figure 1, here a piezo actuator is attached to the beam only. This figure shows that the active stresses counteract the passive stresses. With this damping method the sensor measures the strain in the outer fibers of the flexure [25]. In literature optimization on this type of active damping is done by looking at the location of the collocated damping patch [7, 30], and by considering the controller used [29]. In the location optimizations it is seen that active damping is most effective when it is located at the highest strain energy locations, unconditionally [14].

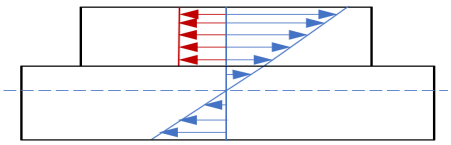

Fig. 1: A schematic overview of the stress in the beam and piezo actuator. In blue are the bending stresses and in red the active stress generated by the actuator

In literature the ratio of damping over weight is optimized even further by combining the damping methods, to use all methods optimally. Those papers elaborate the effect of applying damping methods side-to-side, without optimization of damping performance [28]. Or those elaborate how passive damping can be used to support active damping [4, 31].

The novel hybrid method introduced in this paper combines the subjects of optimizing individual damping methods with developing a hybrid damping layout. This is done through selecting the most suitable

optimized damping method per eigenfrequency, to consecutively combine those to damp all eigenfrequencies considered. An example of a resulting hybrid lay-out is shown in figure 2. In this example the AD patch could be optimized for the $1^{st}$ eigenfrequency and the CLD patch for damping the $2^{nd}$ eigenfrequency. Those are combined to obtain a hybrid mechanism damping the $1^{st}$ an $2^{nd}$ eigenfrequency as effective as possible.

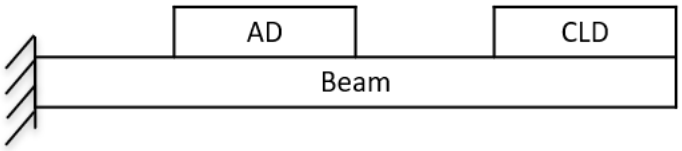


Fig. 2: A schematic example of the proposed hybrid damping mechnism for two eigenfrequencies

The novelty of this paper is the elaboration of all properties influencing damping performance of the individual, and hybrid combination of damping methods. This approach offers as benefit an insight in the properties influencing damping performance. This new gained insight is used to develop a methodology on optimizing a hybrid damping mechanism for a generic one-dimensional structure, including rules-of-thumb aimed at simplifying the optimization approach. This research does not look at optimization of the control technique, since this subject is discussed in a variety of papers [25, 29, 15]. Consequently, a control technique with good damping performance which is relatively easy to implement is used, positive position feedback(PPF) [11]. This control technique is used in industry for its high performance, consequently this technique will enable AD to be used up to full potential [29].
In the first section the paper discusses the preliminary knowledge used, which is an elaboration of the numerical modelling method and of indicators for evaluating damping performance. In the second section hybrid damping will be developed for an example case, which is generalizable to a one-dimensional flexible structure. The third section proves validity of the numerical models used, through comparison with experiments. The discussion discusses how the hybrid method used in section 3.1 is generalized to a methodology for optimization of hybrid damping for a generic case. The methodology introduced includes rules-of-thumb aimed at simplification of the optimization. This section does in the second part discuss why the numerical models used are valid. In the end of the paper a conclusion is given on when and how hybrid damping is beneficial, complemented with recommendations for future research.

## 2 Preliminaries

Two subjects are elaborated to enable the development of hybrid damping for one-dimensional flexures. First a finite element model (FE-model) is developed, since the modelling method used provides information on the limitations of the research. Next, a brief introduction is given on the methods to analyse damping performance. Since development of hybrid damping asks for a comparison of active and passive damping performance. To do this it is needed to differentiate performance measurement indicators.

### 2.1 Structure modelling

For a one-dimensional element the FE-model can be developed via the Euler-Bernoulli approach. This approach is applicable to slender structures only, since it assumes a beam stays perpendicular after deformation [33]. This modelling method is applied to the beam and active damping mechanism directly [6]. However to use it for CLD the method of Mead and Markus will be used [23]. This is needed to account for shear stresses in the viscoelastic layer, neglected by the Euler-Bernoulli approach. The assumptions introduced by those approaches are, the beam is one-dimensional, and the viscoelastic layer of passive damping has a significantly lower Young's modulus than the other layers. Appendices A-C elaborate how to get from the analytical equations to the numerical equations for a single FE-element, for respectively an undamped beam element, a piezo covered beam element and a CLD covered beam element.
The numerical equations of the 3 types of elements are coupled to obtain the intended beam [10]. For example, to obtain a beam coverd for 25% with CLD, three (undamped) beam elements, appendix A, are coupled with one CLD covered beam element, appendix C, figure 3. The elements are coupled according to appendix D.

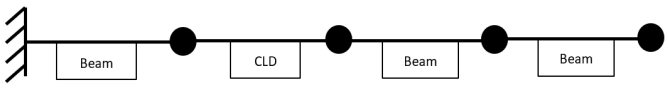


Fig. 3: Coupling elements to obtain a beam which is covered by CLD for 25%

The active damping part needs numerical equations for the transducers, representing the conversion of electrical to mechanical energy and vice-versa. In those equa-

tions the sensor converts strain to a voltage ($\frac{V_{sensor}}{\overline{u}_{sensor}}$), and the actuator that voltage to a stress ($\frac{F_{act}}{V_{act}}$) [6]. The numerical approximations will be elaborated in appendices E and F for the actuator and sensor respectively. The output voltage generated by the sensor is fed to the actuator through a controller. In this research a PPF controller ($H_{controller}$) is placed in between the sensor output and actuator input voltage, for the reasons given in the introduction. Implementation of this controller is elaborated in appendix G. All together this leads to the control-loop of AD as shown in figure 4, elaborated in appendix H. In the figure Y(s) is the matrix representing the transfer function (tf) of the beam ($\frac{\overline{u}}{F}$).

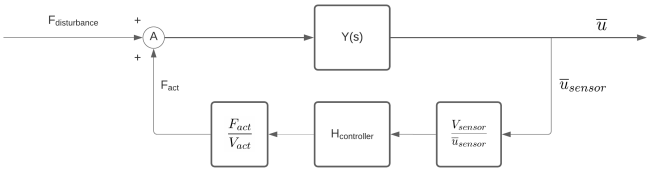


Fig. 4: Block diagram for active damping, closed-loop frequency response

## 2.2 Damping performance evaluation

A conventional manner to analyse damping performance is through analysing the loss factor of the system, $\eta_{system}$. This loss factor is the ratio of strain energy dissipated per cycle over the total amount of strain energy, equation 1 [8].

$$\eta_{system} = \frac{U_{damped}}{U_{system}} \tag{1}$$

Another method to determine the loss factor is to evaluate the damping quality factor (Q-factor), which is a useful method to evaluate active damping performance [32]. Since this method determines the loss factor through the frequency response function (frf) of the closed-loop system, by using a 3dB margin [32].
The resulting loss factor, $\eta_{system}$, is a performance indicator valid for any kind of damping, this makes it applicable for comparison of active and passive damping. However, the method is elaborate for application in location optimization, since it uses information on energy distribution and energy loss. For optimization it is needed to know the relative performance only, being the energy distribution. This means for both types of damping it is sufficient to calculate the amount of strain energy in the damping layer(s) over that in the whole system, $\phi_{system}$ [16]. For example, for figure 8 equation 2 provides $\phi_{system}$ for passive damping and for figure 14 equation 3 provides $\phi_{system}$ for active damping. In those equations $U_n(x)$ represents the strain energy in layer n at length x, in which x is a value between 0 and dL. The higher $\phi_{system}$, the higher the performance. However, this ratio can be used to compare the performances within a damping method only, due to the fact energy loss is not taken into account.

$$\phi_{system} = \frac{\int_0^{dL} U_v(x)dx}{\int_0^{dL} U_b(x) + U_c(x) + U_v(x)dx} \tag{2}$$

$$\phi_{system} = \frac{\int_0^{dL} U_p(x)dx}{\int_0^{dL} U_b(x) + U_p(x)dx} \tag{3}$$

# 3 Location optimized hybrid damping

Two subjects are explored to develop the location optimized hybrid damping mechanism. First the passive and active damping mechanisms are analysed individually. Next, analysis is performed on the influence the optimized methods have on each other, when applied to the same flexible structure in parallel. Those subjects together form the basis to development of hybrid damping, since all properties of influence are considered through this apporach. The optimization is presented through an example case, a cantilever beam with transversal eigenmodes as shown in table 1. This example represents a generic one-dimensional case, since the ratio beam thickness over length is small. This makes the conclusions drawn for this example extendable to all other one-dimensional cases.
Damping of this system is analysed through considering the beam tip displacement as function of force disturbance at the root, this system is visually shown in figure 5. Elaboration of the system will be done in a visual manner, since this will give insight in the properties of influence. This insight will enable future users to extend this research to other one-dimensional cases.

| Eigenfrequency | 1 | 2 | 3 | 4 |
|---|---|---|---|---|
| Frequency [Hz] | 20 | 125 | 345 | 670 |

Tab. 1: Approximate eigenfrequencies cantilever beam

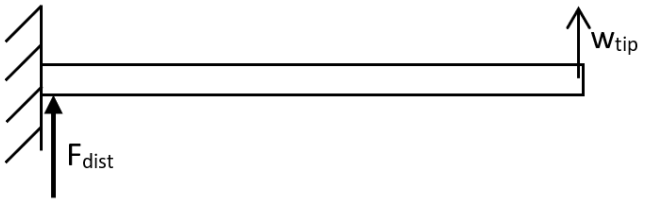


Fig. 5: Schematic visualization of the flexure analysed

## 3.1 Optimization of individual damping methods

The models and evaluation methods introduced in section 2, are used to find the most optimal damping layouts. This means two different numerical models are analysed, one with passive damping added to the structure and one with active, as schematically shown in figures 6 and 7 respectively.

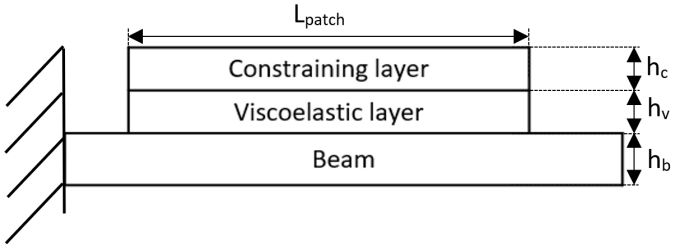


Fig. 6: Schematic visualization of a beam covered with a CLD patch

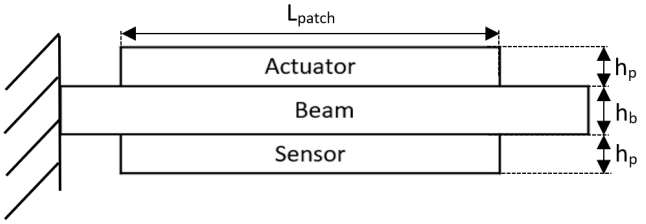


Fig. 7: Schematic visualization of a beam covered with active patches, sensor and actuator

### 3.1.1 Passive damping

Passive damping performance is dependent on several geometrical properties, such as the location of the damping patch, the length of the damping patch, and constraining and viscoelastic layer thickness. On top of that, those geometrical properties are a function of the material properties of the layers. All those influences are explored individually, to obtain insight in those. The geometrical layout of a CLD covered beam element is shown in figure 6. This figure shows a beam($h_b$) covered by a CLD patch, with a constraining ($h_c$) and viscoelastic layer ($h_v$).

**Patch location** The damping effectiveness development of CLD as function of damping patch location is analysed in figure 8. In here three different patch locations are visualized, figures 8a-8c. Those figures visualize the strain energy development for the $2^{nd}$ eigenfrequency per layer, in here the strain energies for the 3 layers are given individually ($h_b$,$h_c$ and $h_v$). This figure shows that multi-peak coverage offers a significantly different strain energy-distribution than single peak coverage, through the viscoelastic and constraining layers, figure 8a compared to figures 8b and 8c. Also it shows that the most effective location for single peak coverage is a CLD patch centered around the tip of the strain energy peak, figure 8c. Appendix I elaborates how this visualization is developed, what assumptions were used, and how this data is processed via the equations from the preliminaries. Also figure 8 shows the modeshapes of the beam when it is covered by CLD, and when it is not covered by CLD, the undamped beam. In those sub-figures it is seen that applying CLD to a beam will slightly change the modeshape of the structure. This influence on modeshape will be elaborated in section 3.2.1 further.

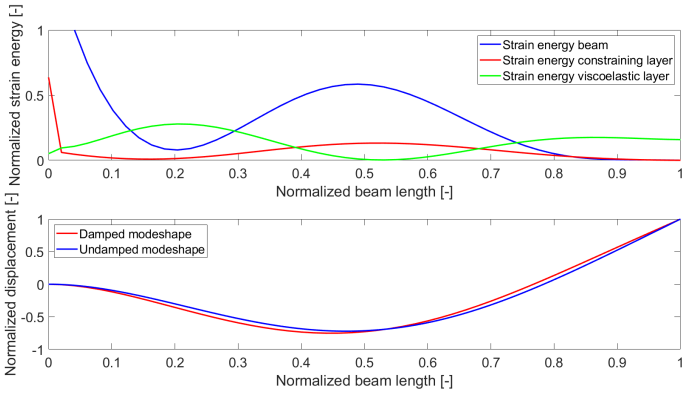


(a) Stress distribution through fully covered CLD beam.

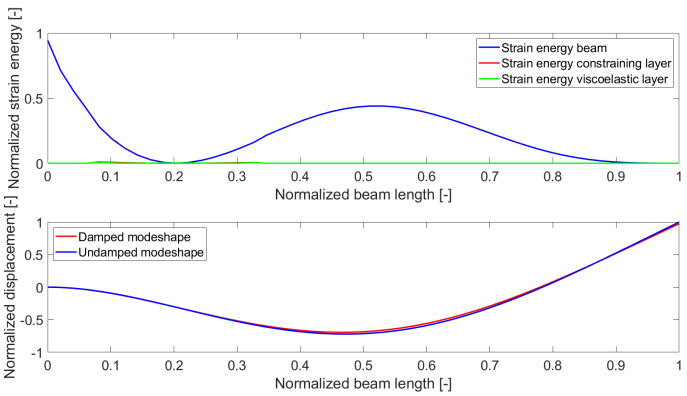


(b) Stress distribution with 25% of the beam covered with CLD, at location of highest strain energy in visoelastic material, from 0.1 - 0.35 on the x-axis

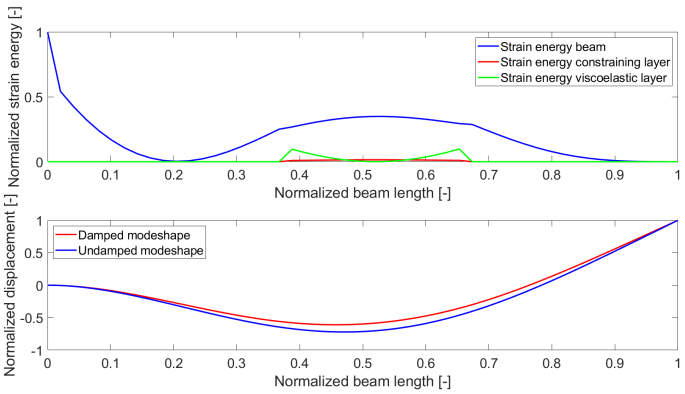


(c) Stress distribution with 25% of the beam covered with CLD, at location of highest strain energy in structure

Fig. 8: Stress through structure partially covered with CLD

To show the dependency of effective patch location on material properties, table 3 is used. In this table 4 types of off-the-shelf viscoelastic materials are compared, of which the viscoelastic material properties are shown in table 2. The viscoelastic materials are constrained by a constraining layer of thickness $h_c = 0.5[mm]$. From table 3 it is concluded that the most effective location is independent of the viscoelastic material properties. So having a patch centered around a strain energy peak is most effective, when just one strain energy peak can be covered, figure 8c. On top of that it is shown, materials with a high shear modulus can be equally effective for single strain energy peak coverage and full beam coverage, C-1002-01 in table 3. Appendix J elaborates how the loss factors are calculated via the formulas introduced in the preliminaries.

| | $G_v$ [MPa] | $h_v$ [mm] |
|---|---|---|
| ISD113 [1] | 0.8 | 0.508 |
| ISD112 [2] | 3 | 0.254 |
| C-1002 - 01 [12] | 20 | 0.381 |
| C-1002 - 03 [12] | 20 | 0.762 |

Tab. 2: Properties of 4 off-the-shelf viscoelastic materials at $20°C$ and 100-150Hz

| | Full coverage (figure 8a) | Highest strain viscoelastic (figure 8b) | Highest strain structure (figure 8c) |
|---|---|---|---|
| ISD113 [1] | 0.0795 | 0.0077 | 0.0232 |
| ISD112 [2] | 0.0698 | 0.0198 | 0.0495 |
| C-1002 - 01 [12] | 0.0444 | 0.0327 | 0.0485 |
| C-1002 - 03 [12] | 0.0634 | 0.0404 | 0.0612 |

Tab. 3: Strain energy distribution $\phi_{system}$ for the second eigenmode at $20°C$ and 100-150Hz

**Patch length** The relation between damping material and patch length ($L_{patch}$) is determined through analysis of the loss factor, $\eta_{system}$. This is done via gradually growing a CLD patch with $h_c = h_v = 0.5[mm]$, around the most effective strain energy peak, and repeating this for different viscoelastic materials. This process is visualized in figure 9, here it is shown at what locations the patches for respectively the $3^{rd}$ and $4^{th}$ eigenfrequency start to grow, and in which direction those symmetrically grow. This method leads to figure 10, here it is shown that different modeshapes have different optimal coverage percentages for the same viscoelastic materials, from damping to weight ratio perspective. Since at certain coverage percentages the growth in loss factor stalls for a while, this differs with shear modulus. More precisely, it shows effectiveness is, among others, a function of the percentage of a strain energy peak the damping patch covers. Since the strain energy peaks cover about 50% and 30% of the beam, for respectively the $3^{rd}$ and $4^{th}$ eigenmode. At those coverages the rise in loss factors start to stall for all shear moduli. The definition strain energy peak used is visually explained in appendix K.

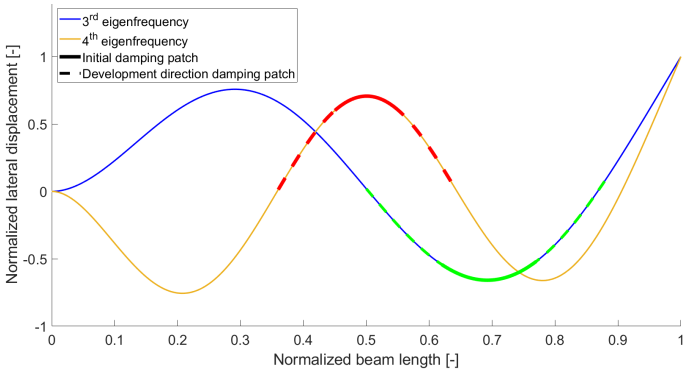


Fig. 9: Visualization of the patch development in figure 10

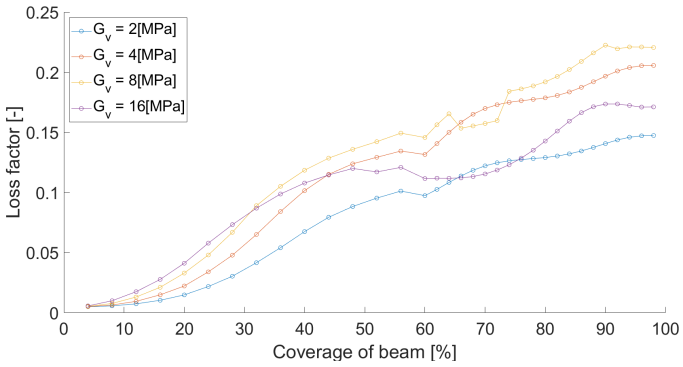


(a) Loss factor ($\eta_{system}$) dependency on patch length for the $3^{rd}$ eigenmode. The patch initially grows symmetrically , as shown in 9, until this is not possible anymore, than it grows towards the object's root only

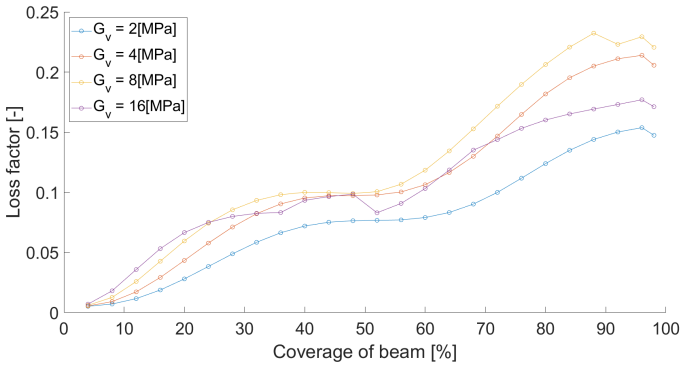


(b) Loss factor ($\eta_{system}$) dependency on patch length for the $4^{th}$ eigenmode. The patch grows symmetrically, as shown in figure 9

Fig. 10: Visualization of loss factor ($\eta_{system}$) dependency on patch length

**Layer thickness** The influence of the constraining and viscoelastic layer thickness on damping performance is determined through an optimization, shown in figure 11. This figure shows the influence layer thicknesses have on the most effective patch length, when the patch is at the most optimal location, shown in figure 19. Figure 11 shows that the thicknesses of the layers determine the slope of the graph, since thicker layers ($h_v$ and $h_c$) will lead to a steeper slope. Consequently thicker layers can lead to higher loss factors. However, figure 11b shows the slope starts to stall at a certain coverage percentage, which is seen in figure 10 earlier.

Increasing the layer thickness of the constraining layer is most effective when the constraining layer is thin compared to the viscoelastic layer, figure 11a. However, increasing the thickness of the viscoelastic layer is most effective when the layer is thick compared to the constraining layer, figure 11b. Since the figures show that doubling layer thickness has no linear relation with the loss factor increase. Consequently, it is expected that an optimal ratio between those layers can be found, this will be case specific in a large extend.

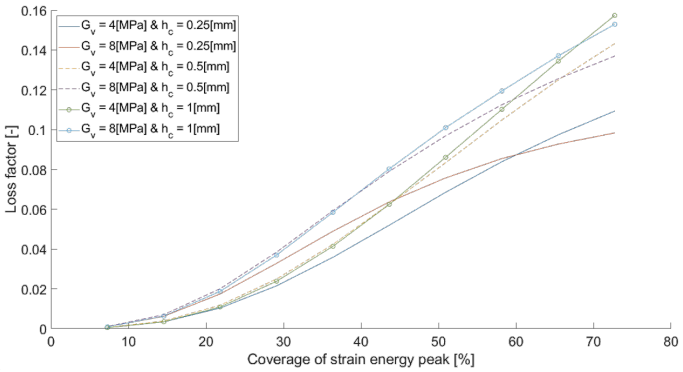


(a) Loss factor ($\eta_{system}$) dependency on patch length and $h_c$

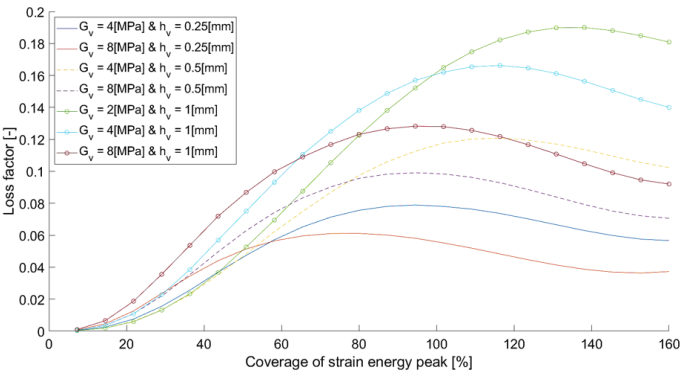


(b) Loss factor ($\eta_{system}$) dependency on patch length and $h_v$

Fig. 11: Loss factor ($\eta_{system}$) dependency on patch length and layer thickness for the $2^{nd}$ eigenmode

All together it is seen that all properties of influence are correlated, which makes it hard to develop a generalized optimization model. However, the visualisations of the damping performance developments offer the opportunity to simplify the passive damping optimization process, this will be done in section 3.3.

### 3.1.2 Active damping

For optimization of active damping the length of the patch is considered only. Since the material properties and thickness of the transducer determine stiffness and force limitations only. To determine the most effective length of the piezo patch an optimization run is executed, as shown in figure 12. In this figure the loss is

represented by the ratio strain energy in the damped flexure over the strain energy in the undamped flexure, the patch length development is handled in a similar manners as in figure 9. In figure 12 an optimization run has been performed for the $3^{rd}$ eigenmode, here it is shown a patch is most effective when it covers between 10-20% of the structure. After 10% coverage the loss factor increase starts to stall, and after 20% the loss stops rising. Consequently it is not needed to have a patch covering more than 20% of the beam, from a damping to weight ratio perspective.
The coverage percentage of the beam length can be transformed to the coverage percentage of the strain energy peak. This leads to the definition, covering between 20-40% of the strain energy peak will lead to the highest loss over weight ratio for a damping patch.

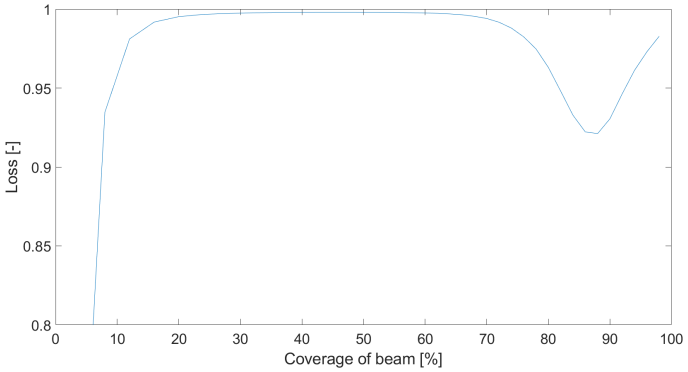


Fig. 12: Loss development as a function of patch length, for the $3^{th}$ eigenmode

The performance development seen for the $3^{rd}$ eigenmode is representable for all other modes. Since it is shown that the stress distribution through the piezo layer follows the same pattern as the one through the main flexure, figure 14. In this figure the strain energy distributions through the beam and piezo layer ($h_p$) are visualized, figure 7. From the distribution as shown in figure 14 it can be concluded that the stress distribution ratios ($\phi_{system}$) are similar for all strain energy peaks of all eigenmodes. Consequently damping performance will develop in a similar manner for all strain energy peaks, eigenmode independent. Thus the 20-40% coverage is valid for all strain energy peaks. Only the $1^{st}$ eigenmode is not considered in this statement, since this eigenmode does not have a strain energy peak. For this reason it is needed to optimize for this mode individually, as shown in figure 13. In this figure it is shown that a patch designed for the $1^{st}$ eigenfrequency needs a coverage percentage of 10-20% of the beam, to be most effective.

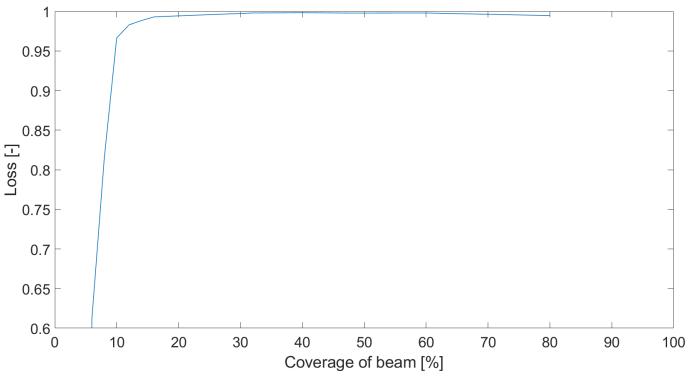


Fig. 13: Loss development as a function of patch length, for the $1^{st}$ eigenmode

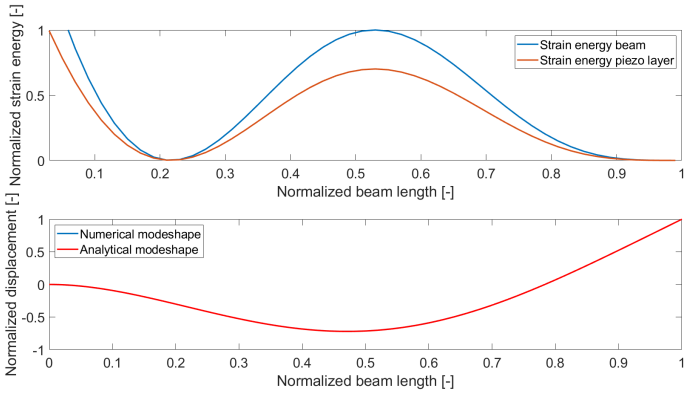


Fig. 14: Stress distribution with the beam fully covered by a piezo element

## 3.2 Influence of the hybrid damping lay-out

The optimized damping methods will be applied to the flexure as local damping method, as shown in figure 2. Those damping methods can change the dynamic properties of the structure in two manners, those can cause a change in modeshape and in eigenfrequency. Those effects are caused by the local stiffness change introduced to the structure.

### 3.2.1 Modeshape manipulation

The modeshape will not be manipulated significantly when the damping patch applied is symmetrically distributed around a strain energy peak, figure 8c. Since this figure shows the height of the displacement peak is reduced only. However, when the damping patch is not symmetrically distributed around a strain energy peak, and when it is still located at a high strain energy location, than the modeshape change can be more significant due to a shift in the location of the displacement peak, figure 8a. Having this more significant modeshape change can influence damping performance. For this reason this section will discuss the

influence a damping patch designed for the $3^{rd}$ eigenfrequency has on the modeshape of the $2^{nd}$ eigenfrequency. This example can be generalized to all eigenfrequencies, because this modeshape influence will be the most significant one. Since the larger the local stiffness increase the larger the influence on modeshape. This stiffness increase is a function of the size of the patch and the strain at the specific location. Regarding the patch size, it is known that the effectiveness of a damping patch is a function of the percentage strain energy peak it covers, section 3.1. Consequently a lower eigenfrequency needs a larger damping patch to obtain similar damping effectiveness. So the $2^{nd}$ eigenfrequency needs the largest patch followed by the $3^{rd}$ eigenfrequency. However, the influence the optimized patch for $3^{rd}$ eigenfrequency has on the modeshape of the $2^{nd}$ eigenfrequency is larger than vice-versa. Since the $3^{rd}$ mode patch is at a higher strain energy location for the $2^{nd}$ mode than vice-versa, as schematically shown in figure 15. This figure shows that the curvature experienced by the green patch is larger than that experienced by the black patch. Thus the situation considered in this analysis will experience the largest influence by a damping patch, consequently the largest modeshape change.

For active damping, the stress distribution through the active damping layers is the same as the one through the beam. This means at the location of the piezo patch the curvature of the beam is reduced with a continuous factor. Consequently the change in modeshape is small, as shown in figure 16. This figure shows the strain energy in the beam and piezo layer ($h_p$), as schematically shown in figure 7. With passive damping the strain energy distributions are not similar, this means the curvature will change with a discontinuous factor. This results in a modeshape in which the location of the peak has shifted more significantly, as shown in figure 17.

Both methods do influence the modeshape of the beam, a modeshape change introduced by passive damping is larger than by active damping. However, the situation shown in this section is the worst case situation, and even in this situation the modeshape changes are small. Consequently it is not needed to consider the modeshape changes, as long as the added damping layers are thin compared to the beam thickness. This is the case when $\frac{h_p}{h_b} \leq 0.26$, since this is the ratio used in this example.

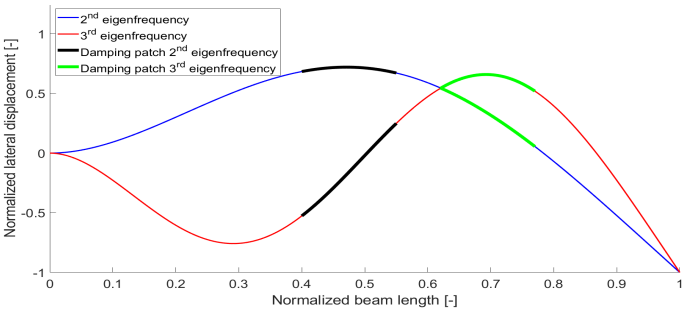


Fig. 15: Influence the damping patches for the $2^{nd}$ and $3^{th}$ eigenmode have on the other eigenmode

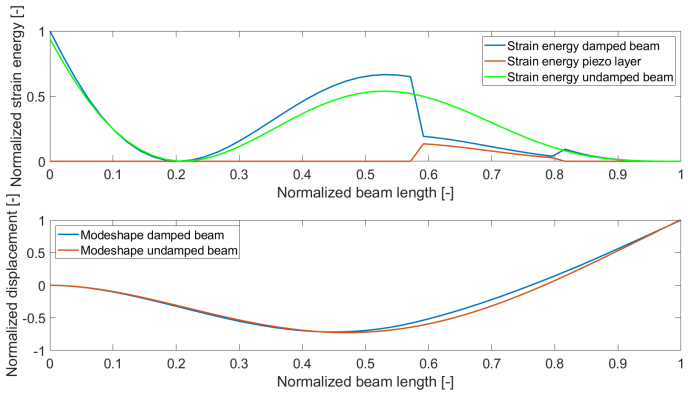


Fig. 16: Influence of piezo patch on the $2^{nd}$ eigenmode, when designed for the $3^{th}$ eigenmode

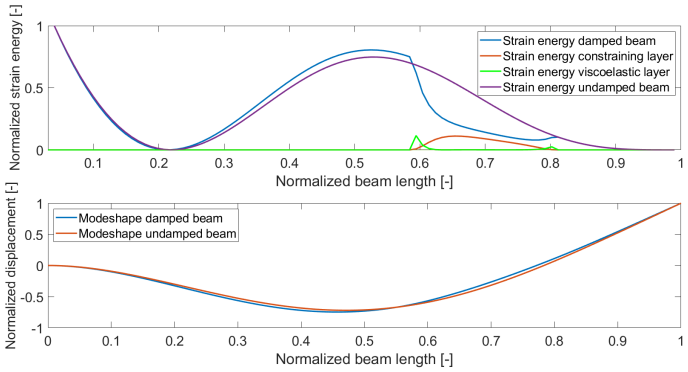


Fig. 17: Influence of CLD patch on the $2^{nd}$ eigenmode, when designed for the $3^{th}$ eigenmode

### 3.2.2 Eigenfrequency manipulation

Adding damping material to the flexure will higher the eigenfrequencies. Especially for the eigenfrequency the specific patch dampens, since here $\phi_{system}$ will be highest.

In the active damping case the controllers have an influence on the location of the eigenfrequencies. However the influence of the controller can be manipulated by tuning the controller parameters. In this case the controller is tuned for optimal damping performance,

consequently frequency shifts can occur.
Figure 18 shows the frequency response function (frf) of the transfer function (tf) $\frac{w_{tip}}{F_{disturbance}}$, as in figure 5, for all cases. Here it can be seen that the frequency shifts are significant for the damped modes, independent of active or passive damping is applied. However, it is shown that both methods do offer a slightly different eigenfrequency shift, in which the frequency shift caused by CLD is generally larger. Also it is shown that the controller of active damping has just a small influence on the eigenfrequencies below the cut-off frequency of the controller, despite the PPF controller properties [29]. This is caused by the fact that the amount of strain energy at the location of the damping patch optimized for the $2^{nd}$ eigenfrequency is little for the $1^{st}$ eigenmode, as can be concluded from the modeshapes shown in figure 19. Thus the actuator has small influence on the $1^{st}$ eigenmode.
From this comparison it is concluded that eigenfrequency shifts need to be considered when hybrid damping is developed. However the importance of it is dependent on the strain energy distribution, $\phi_{system}$, at the location of the damping patch. The higher this value the more important consideration of the eigenfrequency manipulation.

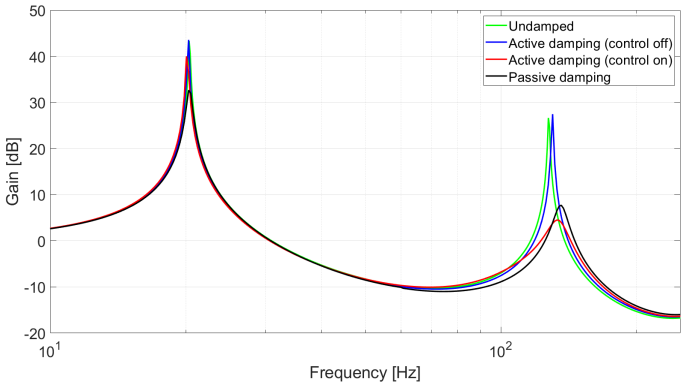


Fig. 18: Eigenfrequencies shifts caused by damping methods

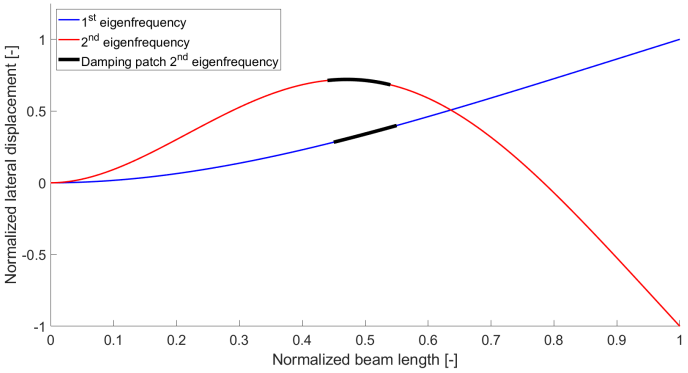


Fig. 19: Visualization of the location of a damping patch designed for the $2^{nd}$ eigenfrequency

## 3.3 Location optimized hybrid damping

The first step in developing hybrid damping for the example case is to determine the weight the damping patches are allowed to have. Defining the weight allowed for each eigenfrequency individually can be beneficial, since the actuator force needed for active damping can differ for all eigenfrequencies, thus different actuator thicknesses are needed. For this reason it is advised to use the weight of the piezo transducers to define the weight a general damping patch is allowed to have.
For active damping patches it is relatively simple to evaluate performance as a function of dimensions. Covering 20-40% of a strain energy peak offers best performance in all cases. And the thickness of the transducers will determine the maximum force the transducers can develop only. This means an estimate has to be made on what thickness transducer is needed to damp a certain eigenfrequency. In the example case a PICeramic P876-A12 transducer was chosen as actuator for all eigenfrequencies. Those were chosen due to its length (matching the piezo length needed) and the fact those patches are relatively thick, thus the force the patches can develop is sufficient, unconditionally. The weight of the sensor is not taken into account by defining the patch weight, since any piezo patch thickness can be used as sensor.
The loss factor offered by an active damping patch is calculated through the Q-factor, as introduced in section 2.2. To determine this factor it is needed to have the PPF controller tuned for optimal performance. Optimal performance will in this case mean achieving the highest amount of damping, while the controls do not dominate the dynamics of the system. Tuning of the controller is shown in appendix L. The optimized patch locations are shown in appendix M. The loss factors and coverage percentages offered by active damping are shown in table 4.

| | Eigenfreq. | | |
|---|---|---|---|
| | $1^{st}$ | $2^{nd}$ | $3^{th}$ |
| $\eta_{system}$ | 0.12 | 0.11 | 0.12 |
| Peak coverage | - | 25% | 40% |

Tab. 4: Loss factor and amount of peak coverage provided by P876-A12 damping patch, for each eigenfrequency(Patch locations are shown in appendix M)

With the weight of the damping patches set, the most optimal CLD lay-out is determined. This is done through finding the highest loss factor in a case specific optimization, as can be concluded from section 3.1.
In this section it was shown passive damping is most effective when it is applied to a strain energy peak of the structure. And the increase in damping performance is not significant when a bit over one peak is covered. This means, at a certain moment increasing layer thicknesses will be more effective than increasing coverage percentages. For this increase it is generally seen that the viscoelastic layer needs to be thicker or equally thick as the constraining layer, as concluded from figure 20. Since here it is shown that the layers have this ratio when CLD has the most effective length.
Due to all case specific properties an optimization as shown in figure 20 needs to be executed. For this optimization the loss factors, $\eta_{system}$, are calculated via equation 1. In the figure it is shown that the best CLD coverage percentage for the $2^{nd}$ eigenmode is 60% of the strain energy peak. And for the $3^{th}$ and higher eigenmodes it is 90%. This means passive damping is most effective when it covers 90% of a strain energy peak, as long as the layers have sufficient thickness. The damping factors for CLD can be summarized as in table 5. The optimized patch locations are shown in appendix M.

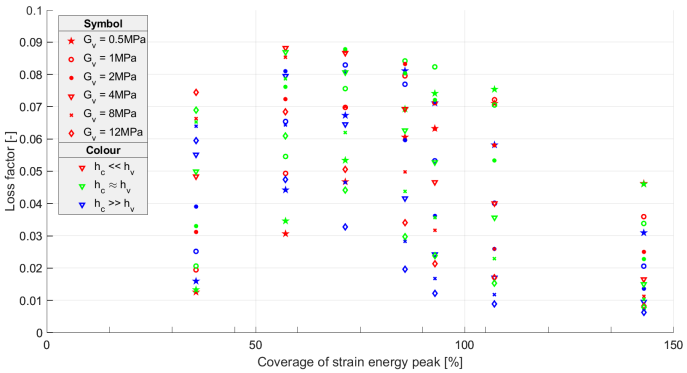


(a) Loss factor, $\eta_{system}$, development for the $2^{nd}$ eigenmode of CLD as function of patch size, lay-out and shear modulus

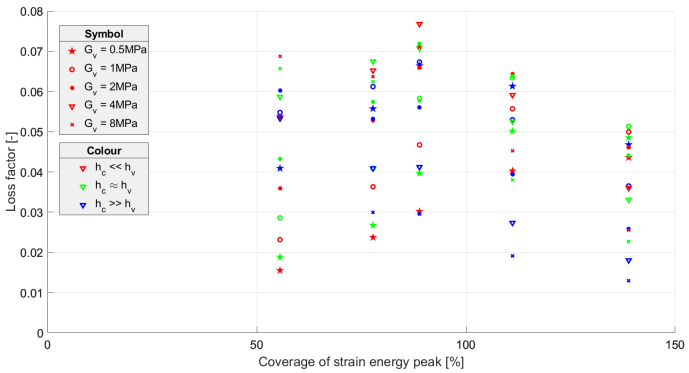


(b) Loss factor development for the $3^{th}$ eigenmode of CLD as function of patch size, lay-out and shear modulus

Fig. 20: Loss factor, $\eta_{system}$, development of CLD as function of patch size, lay-out and shear modulus

| | Eigenfreq. | | |
|---|---|---|---|
| | $1^{st}$ | $2^{nd}$ | $3^{th}$ |
| $\eta_{system}$ | 0.085 | 0.088 | 0.073 |
| Peak coverage | - | 60% | 90% |

Tab. 5: Loss factor and amount of peak coverage provided by a CLD patch, for each eigenfrequency (Patch dimensions are shown in appendix M)

Section 3.2.1 discusses the influence both damping methods have on the modeshape, here it is shown this influence is neglectable in the hybrid damping development approach. Consequently location optimization of a damping patch for a non-hybrid case (the specific patch applied only), figure 2, is representable for a hybrid case with multiple patches, figure 6. Also this means tuning the controller for a non-hybrid case will give a controller representable for the hybrid case. Although, the cut-off frequency of the controller has to be re-tuned for hybrid damping, since the eigenfrequency shifts are significant and damping lay-out dependent. This re-tuning needs to be done from the highest to lowest eigenfrequency, due to the properties of the controller, as discussed in section 3.1.2.
This re-tuning statement is valid when the active damping patch considered does not overlap with CLD patches. Since overlap with a CLD patch will mean a change in force and energy transmissions, leading to a change in optimal controller properties [35]. In that case it would be needed to re-tune all controller parameters. On top of that overlapping patches probably do lead to other optimal patch dimensions. However this influence has not been researched in this paper.
When all eigenfrequencies get the most effective damp-

ing method assigned, it is seen all eigenfrequencies are damped actively for the example case. In case active damping performance is not limited by hardware or force limitations.
Hardware limitations reduce the performance of active damping through low-pass filtering properties mainly. When those limitations get significant, than passive damping starts to outperform active damping for the specific eigenfrequencies. Consequently hybrid damping can offer benefits.
Maximum force wise it is seen active components are used in full extend when the damped amplitudes of the tip displacements are as shown in table 6. In this table 2 configurations of the P876-A12 transducer are shown. The off-the-shelf transducer, which can be used in the -100V to +100V region only. And the optimized transducer, which is the same transducer optimized for an operation region of -250V to +250V. This optimized transducer is shown since in future application active damping will be used in full extend.
Displacements larger than shown in table 6 will need reduction of the controller gain, which consequently reduces the damping abilities. When this is needed, than hybrid damping can achieve similar performance as active damping. This is the case when the $2^{nd}$ eigenmode amplitude is 0.39mm or 0.99mm for the non-optimized and optimized transducers respectively. For larger displacements passive damping is more effective than active damping for the specific eigenfrequency, consequently hybrid damping can offer benefits.

| | Eigenfreq. | |
|---|---|---|
| | $1^{st}$ | $2^{nd}$ |
| $a$ | 1.7mm | 0.28mm |
| $a_{opt}$ | 4.2mm | 0.7mm |

Tab. 6: Tip displacement amplitudes to use active damping in full extend

## 4 Validation

So far all conclusions are based on numerical models. To ensure validity of those models experiments are carried out. The experiments show validity of the models for a case in which the damping methods are location optimized only. This means the experiments will not show the benefits of hybrid damping, but those will show validity of the numerical models only.

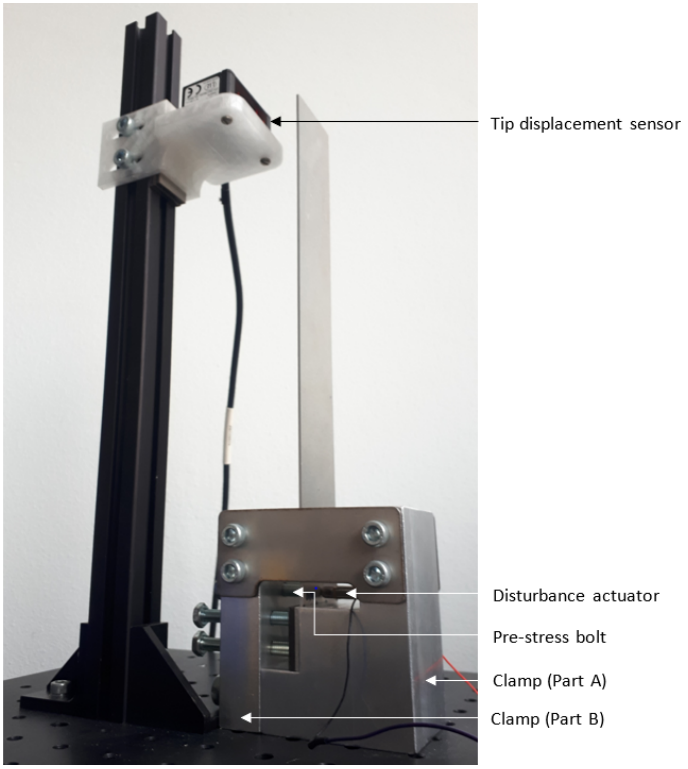


Fig. 21: Picture of the experimental set-up

For the experiments a set-up as shown in figure 21 is used. This figure shows the system is disturbed close to the root, and the vibrations amplitude is measured at the tip of the beam, as schematically shown in figure 5. The clamp is designed with side-plates to ensure sufficient stiffness of part A and B of the clamp, to mimic proper clamping. A pre-stress bolt is used to create a pure sinusoidal disturbance force ($F_{disturbance}$), without damaging the disturbance actuator (PiezoDrive SA050520). This is needed since elongation is a weak stress direction for piezo materials. The tip displacements are measured with 2 types of sensors, for calibration a laser-triangulation sensor (optoNCDT1220-10 [24]) is used and for final measurements a more accurate single point laser vibrometer (Polytech OVF-505). Next, 4 types of beam coverages are placed in this set-up, a non-covered, an optimized active covered, an optimized passive covered and a hybrid covered beam, respectively. For the hybrid system AD is location optimized for the $1^{st}$ eigenfrequency, and CLD for the $2^{nd}$. Since higher modes are most likely to be damped passively, section 3.3. The reason to consider 2 eigenfrequencies only is because all properties considered in section 3 are included with those frequencies already. Consequently the experiments give a reliable validation of the numerical models.
As active components the same transducers as in the numerical models are used, PIceramics P876-A12

transducers [27]. For passive damping the 3M damping foil 2552 is used [3]. The performance of this material is reduced compared to the performance of the optimal CLD lay-out, as derived in the numerical models. Thus the loss factor provided by CLD will not represent the highest loss factor possible in the hybrid damping lay-out. However, due to the viscoelastic material properties does this foil provide significant damping for both eigenmodes, consequently the performance of full CLD coverage is high.

The experiments are carried out by giving the disturbance actuator a frequency sweep from 1-250Hz, this leads to the FRF's as shown in figure 23.

In order to compare the measured data to the models the properties of the experimental set-up need to be analysed. The passive behaviour is analysed by looking at the undamped beam, the CLD covered beam and the beam covered with in-active piezo patches, with this analysis the material properties in the numerical models are tuned. The active behaviour of AD is analysed via the control-loop, shown in figure 22. Here it is shown 5 hardware components can influence AD performance. Of those 5, the actuator, sensor and amplifier are analysed only, since it can be assumed the NI modules have predictable behaviour. The analysis is used to adjust the numerical models to properties similar to the experiments and to mathematically correct for errors. For example, the piezo patch used as sensor for the $1^{st}$ eigenfrequency in the full active damped system has significant transmission losses, probably due to bad wiring or overheating during installation. Those losses are corrected through multiplication with a correction factor. With the analysis of AD it was seen that the amplifiers have varying gains and behave like low-pass filters, consequently damping performance for the $2^{nd}$ eigenmode is limited. The low-pass filtering properties and experimental gains are implemented in the numerical models, to have the same dynamics for the models and the experiments. A more elaborate discussion on the analysis is shown in appendix N.3.

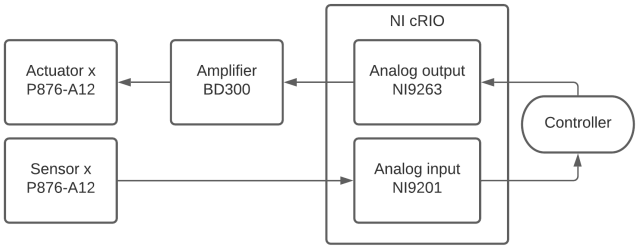


Fig. 22: Visualisation of the AD control-loop

Figure 23a shows the experimental FRF's and figure 23b shows the numerical approximations. Comparison of those figures shows the peaks occur at similar frequencies.

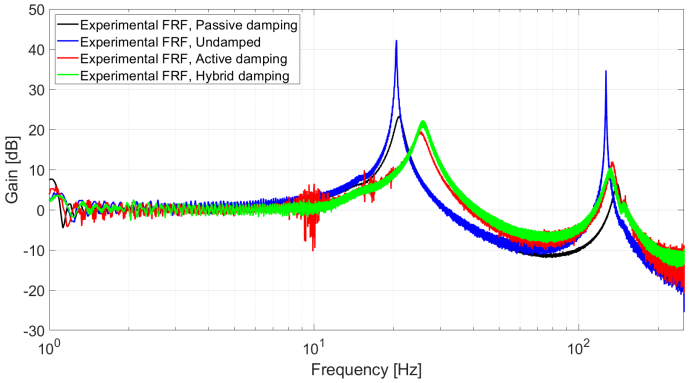


(a) Experimental FRF

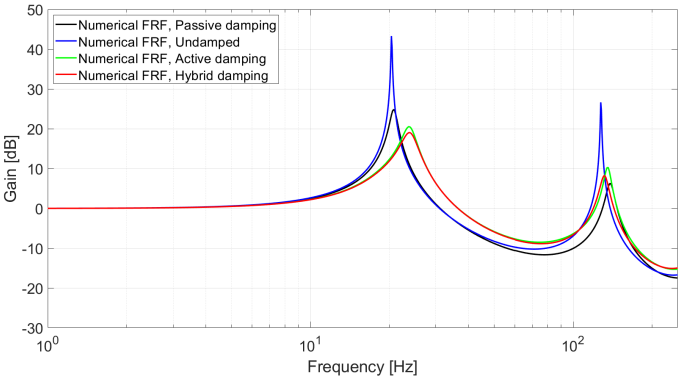


(b) Numerical FRF

Fig. 23: The FRF's of the experiments and numerical predictions

Besides validation of the locations of the eigenfrequencies do the experiments also provide the loss factors for all the damping methods, as shown in table 7. In the table it is shown the loss factors are similar too. The loss factors are calculated through the Q-factor, as introduced in section 2.2.

A more elaborate explanation on how the experiments are carried out is shown in appendix N.

| | $1^{st}$ eigenfreq. | | $2^{nd}$ eigenfreq. | |
|---|---|---|---|---|
| Damping type | $\eta_{exp}$ | $\eta_{num}$ | $\eta_{exp}$ | $\eta_{num}$ |
| Active | 0.12 | 0.12 | 0.058 | 0.059 |
| Passive | 0.076 | 0.073 | 0.063 | 0.069 |
| Hybrid | 0.12 | 0.13 | 0.076 | 0.080 |

Tab. 7: Comparison of the loss factor for the experimental and numerical approach, $\eta_{exp}$ and $\eta_{num}$ respectively

# 5 Discussion

Two subjects are discussed in this section, the first subsection discusses how the knowledge gained through the example case, section 3.3, is used to develop a methodology on development of hybrid damping for all one-dimensional cases. The second part of this section discusses why the experiments prove validity of the numerical models and approach used.

## 5.1 Hybrid damping development methodology

The example case of section 3.3 can be extended to a general case, thus an approach plan to obtain hybrid damping is developed, figure 24. The figure shows an unconditional valid methodology to develop hybrid damping for a system in which it is known which eigenfrequencies need to be damped, when the damping patches do not overlap and when the damping layers are thin compared to the beam thickness. This methodology aims at designing hybrid damping mechanisms in which the allowable weight increase by the damping patches is determined upfront. This is different from a methodology aiming at achieving a predefined loss factor. Since in the approach used it is not known what the final loss factors will be, however this does mean the ratio of loss factor over weight will be optimized.
Assigning the damping methods to eigenfrequencies is done in the order from highest to lowest frequency. This has two reasons. One is when for a specific eigenfrequency it is seen hardware limitations are the main contributors causing passive damping to outperform active damping. Than it can be concluded, as soon as active damping outperforms passive damping, all lower eigenfrequencies need active damping. Since the influence of hardware limitations increases with frequency [29]. The other reason is the fact PPF can cause frequency shifts for frequencies below the cut-off frequency. Consequently it is needed to re-tune the controllers in the order from highest to lowest eigenfrequency.

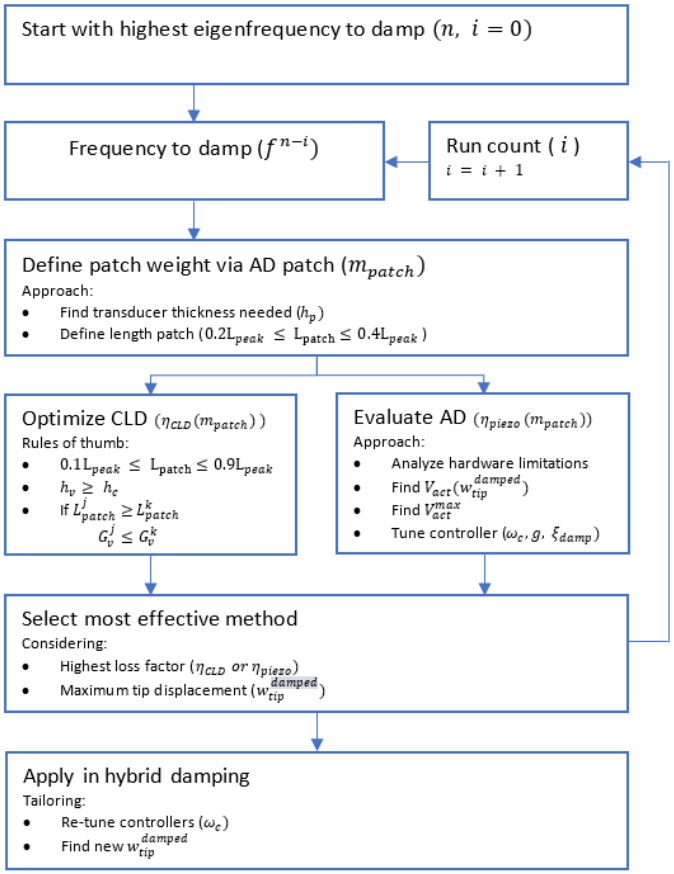


Fig. 24: Methodology to develop hybrid damping

Several steps are taken per individual eigenfrequency. First the weight of the damping patch is defined, via the properties and dimensions allowed for AD. With the weight of a general damping patch, AD or CLD, defined the individual damping methods can be optimized. For optimization of CLD 3 rules-of-thumb are given, which all are deviated from section 3.1.1. Those rules are used to give direction to the optimization. Those rules state, the patch covers a certain part of the strain energy peak, the viscoelastic layer needs to be thicker or equally thick as the constraining layer. And the shear modulus needs to be higher when a higher eigenfrequency is being damped, only if the damping patch has gotten smaller.
For optimization of AD it is needed to estimate the actuator force required, through analyzing the amplitude of the eigenmode. This together with the hardware limitations will define the boundaries in which AD can perform optimally. Also for AD it is needed to optimize the PPF-controller, to achieve optimized damping.
The next step is to select the best damping method for the specific eigenfrequency, and evaluate if the amplitude of the mode is damped sufficiently. When those steps are followed for each eigenfrequency and when

the patches are applied in the hybrid system, than the controllers for the AD patches need to be re-tuned. And the amplitudes have to be evaluated one last time, since combining the methods will change the amplitudes slightly, as seen for the AD patches for the $1^{st}$ eigenfrequency in figure 23.
It needs to be noted, when damping patches do overlap, than re-tuning of all controller parameters would be needed for the specific active patches. This re-tuning dependents on how this overlap is managed physically. Also overlap can cause the optimized damping lay-outs to be not optimal for the new hybrid system anymore. Due to the fact they were optimized for a non-overlapping patches lay-out. Consequently, for this case it is needed to extend the methodology.

## 5.2 Validation of numerical models

By comparing figure 23a and figure 23b and looking at table 7 the first thing to notice is, the experiments and numerical models give similar results. However, several small differences can be seen.
For the $1^{st}$ eigenmode the AD system has a higher peak than the hybrid damped system, for the experiments, however for the numerical models it is vice-versa. This means there is a mis-match in piezo material properties or amplifier gains probably.
For the $2^{nd}$ mode all curves have a small extra peak in the experimental data. Probably this is caused by a flaw in the clamp.
All together, the models give reliable results for a one-dimensional flexible structure, for all three damping methods. Thus the approach introduced can be used for development of hybrid damping mechanisms for one-dimensional flexible structures.

## 6 Conclusion

This novel location optimized hybrid damping method will improve the damping performance for a one-dimensional structure, in case the amplitudes of the eigenmodes are large or in case hardware limitations limit the performance of active damping. To develop this newly introduced damping method the approach as summarized in figure 24 can be used. With this methodology the benefits of both damping techniques will be used in full extend, which leads to an improved damping over weight ratio for one-dimensional flexible structures.

## 7 Recommendations

This paper offers a methodology to develop hybrid damping for one-dimensional flexures, however this methodology contains several simplifications and assumptions. The methodology considers a system in which damping patches do not overlap, however when a large frequency bandwidth is damped, than overlap between patches will occur. To account for this the methodology has to be extended.
It is expected in several hybrid damping development processes it will be the case that as soon as active damping outperforms passive damping, than all lower eigenfrequencies need to be damped actively. However, a more elaborate research has to be carried out, to find rules-of-thumb for when this is the case.
This method considers one individual damping method per eigenfrequency only. However, using a hybrid damping method, active and passive damping combined, for one individual eigenfrequency, could be beneficial in some cases [4, 31]. For this reason it could be beneficial to make a comparison between the 3 damping methods per eigenfrequency.
When more knowledge is gained in this area, than this method can be applied in 'MetaMech'. This is a project at Delft university of technology researching the benefit of constructing a flexure out of damping elements, those elements can be active, hybrid or passive. Developing a methodology to select which eigenfrequency is damped by which damping method at what location, can be key to development of the most effective 'MetaMech' structure possible.

## References

[1] 3M™. Layered Viscoelastic Damping Polymer (SJ-2040X), 2017.

[2] 3M™. Viscoelastic Damping Polymer 112 Series, 2017.

[3] 3M Industrial Business. Damping Foil 2552, 2012.

[4] A. L. Araújo, P. Martins, C. M. Mota Soares, C. A. Mota Soares, and J. Herskovits. Damping optimisation of hybrid active-passive sandwich composite structures. *Adv. Eng. Softw.*, 46(1):69–74, 2012.

[5] S. Assaf, M. Guerich, and P. Cuvelier. Vibration and damping analysis of plates with partially covered damping layers. *Acta Acust. united with Acust.*, 97(4):553–568, 2011.

[6] A. Baz and J. Ro. Vibration control of plates with

active constrained layer damping. *Smart Mater. Struct.*, 5(3):272–280, 1996.

[7] Y. Belkourchia, L. Azrar, and E. S. M. Zeriab. Hybrid optimization procedure and active vibration control of beams with piezoelectric patches. *Proc. 2018 Int. Conf. Optim. Appl. ICOA 2018*, (1):1–7, 2018.

[8] A. Bhimaraddi. Sandwich beam theory and the analysis of constrained layer damping. *J. Sound Vib.*, 179(4):591–602, 1995.

[9] Y. C. Chen and S. C. Huang. An optimal placement of CLD treatment for vibration suppression of plates. *Int. J. Mech. Sci.*, 44(8):1801–1821, 2002.

[10] D. De Klerk, D. J. Rixen, and S. N. Voormeeren. General framework for dynamic substructuring: History, review, and classification of techniques. *AIAA J.*, 46(5):1169–1181, 2008.

[11] A. J. den Hamer, G. Z. Angelis, and N. B. Roozen. Multi-mode adaptive positive position feedback: An experimental study. *J. Sound Vib.*, 19(2):438–455, 2014.

[12] E.A.R. shock and Vibration. Engineering Design Guide.

[13] G. Fabbrocino, G. Manfredi, and E. Cosenza. Non-linear analysis of composite beams under positive bending. 70:77–89, 1999.

[14] M. I. Friswell. Partial and segmented modal sensors for beam structures. *JVC/Journal Vib. Control*, 5(4):619–637, 1999.

[15] P. Gaudenzi, R. Carbonaro, and E. Benzi. Control of beam vibrations by means of piezoelectric devices: Theory and experiments. *Compos. Struct.*, 50(4):373–379, 2000.

[16] R. V. Grandhi and D. E. Veley. Effect of number of actuators on optimum actively controlled structures. *Eng. Optim.*, 19(1):51–63, 1992.

[17] S. C. Huang, D. J. Inman, and E. M. Austin. Some design considerations for active and passive constrained layer damping treatments. *Smart Mater. Struct.*, 5(3):301–313, 1996.

[18] H. Janocha. *Adaptronics and smart structures*. Springer Berlin Heidelberg New York, 2 edition, 2007.

[19] E. M. Kerwin. Damping of Flexural Waves by a Constrained Viscoelastic Layer. *J. Acoust. Soc. Am.*, 31(7):952–962, 1959.

[20] N. Kumar and S. P. Singh. Vibration and damping characteristics of beams with active constrained layer treatments under parametric variations. *Mater. Des.*, 30(10):4162–4174, 2009.

[21] C. Lee and F. C. Moon. Laminated piezopolymer plates for torsion and bending sensors and. *J. Acoust. Soc. Am.*, 85(1989):2432, 1989.

[22] P. Lewis and J. Ward. The finite element method. *Princ. Appl. Addison-Wesley*, 1991.

[23] D. Mead and S. Markus. The forced vibration of a three-layer, boundary damped sandwich beam with arbitrary boundary conditions. *Sound Vib.*, 10(2):163–175, 1969.

[24] Micro-Epsilon. optoNCDT 1220, 2010.

[25] S. O. R. Moheimani and a. J. Fleming. *Piezoelectric transducers for vibration control and damping (advances in industrial control)*. 2006.

[26] R. A. Moreira, J. D. Corte-Real, and J. D. Rodrigues. A generalized frequency-temperature viscoelastic model. *Shock Vib.*, 17(4-5):407–418, 2010.

[27] PI Ceramic GmbH. Piezo technology.

[28] J. Plattenburg, J. T. Dreyer, and R. Singh. Active and passive damping patches on a thin rectangular plate: A refined analytical model with experimental validation. *J. Sound Vib.*, 353:75–95, 2015.

[29] A. Preumont. *Vibration control of active structures*, volume 179. 2011.

[30] K. Ramesh Kumar and S. Narayanan. Active vibration control of beams with optimal placement of piezoelectric sensor/actuator pairs. *Smart Mater. Struct.*, 17(5), 2008.

[31] J. Ro and A. Baz. Optimum placement and control of active constrained layer damping using modal strain energy approach. *JVC/Journal Vib. Control*, 8(6):861–876, 2002.

[32] W. Siebert. *Circuits, signals, and systems*. MIT press, 1986.

[33] G. Singer, Y. Measho, and A. Mahmood. Modelling and control of a flexible structure. *IEE Colloq.*, (42), 1996.

[34] M. A. Trindade. Experimental analysis of active-passive vibration control using viscoelastic materials and extension and shear piezoelectric actuators. *JVC/Journal Vib. Control*, 17(6):917–929, 2011.

[35] M. A. Trindade and A. Benjeddou. Hybrid active-passive damping treatments using viscoelastic and piezoelectric materials: Review and assessment. *JVC/Journal Vib. Control*, 8(6):699–745, 2002.

# Appendices

## Nomenclature

| | |
|---|---|
| $\epsilon_{piezo}$ | Permittivity piezo material |
| $\rho_b$ | Density beam |
| $\rho_c$ | Density constraining layer |
| $\rho_p$ | Density piezo material |
| $\rho_v$ | Density viscoelastic layer |
| A | Cross-sectional area |
| $A_b$ | Cross sectional area beam |
| $A_c$ | Cross sectional area constraining layer |
| $A_p$ | Cross sectional area viscoelastic layer |
| $A_v$ | Cross sectional area viscoelastic layer |
| b | Width beam |
| $b_c$ | Width constraining and viscoelastic layer |
| $b_p$ | Width of piezo transducer |
| $C_p$ | Capacitance of piezo-element |
| $dL$ | Length of one element |
| $d_{31}$ | Piezo electric charge constant |
| $E_b$ | Youngs modulus beam |
| $E_c$ | Youngs modulus constraining layer |
| $E_p$ | Youngs modulus piezo material |
| $G_e$ | Equivalent Shear Modulus |
| $G_v$ | Shear modulus viscoelastic material |
| $g_{31}$ | Piezo electric voltage constant |
| $h_b$ | Thickness beam |
| $h_c$ | Thickness constraining layer |
| $h_g$ | Thickness glue layer |
| $h_p$ | Thickness glue layer |
| $h_v$ | Thickness viscoelastic layer |
| $I_b$ | Second moment of area beam |
| $I_c$ | Second moment of area constraining layer |
| $I_p$ | Second moment of area constraining layer |
| $K_b$ | Stiffness matrix undamped/bare beam element |
| $K_{CLD}$ | Stiffness matrix beam element covered with CLD |
| $K_{piezo}$ | Stiffness matrix beam element covered with piezo transducers |
| $k_{13}$ | Coupling factor piezo material |
| L | Element length |
| $M_b$ | Mass matrix undamped/bare beam element |
| $M_{CLD}$ | Mass matrix beam element covered with CLD |
| $M_{piezo}$ | Mass matrix beam element covered with AD |
| $N_w$ | Shape function lateral displacement |
| $N_b$ | Shape function axial displacement beam element |
| $N_c$ | Shape function axial displacement constraining layer |
| $N_p$ | Shape function axial displacement piezo element |
| $N_v$ | Shape function axial displacement viscoelastic layer |
| $S^e_{11}$ | Compliance piezo material |
| $T$ | Kinetic energy |
| $T_b$ | Kinetic energy beam |
| $T_c$ | Kinetic energy constraining layer |
| $T_v$ | Kinetic energy viscoelastic layer |
| $U$ | Strain energy |
| $U_{Damping}$ | Strain energy in damping layer |
| $U_{Damped}$ | Dissipated energy by damping layer |
| $U_{System}$ | Strain energy in whole system |
| $U^n_b$ | Strain energy in the beam at element n |
| $U^n_c$ | Strain energy constraining layer, element n |
| $U^n_v$ | Strain energy viscoelastic layer, element n |
| $u_b$ | Axial displacement beam |
| $u_c$ | Axial displacement constraining layer |
| $u_p$ | Axial displacement piezo layer |
| $V_{act}$ | Voltage piezo actuator |
| $V_{in}$ | Input voltage amplifier |
| $V_{sensor}$ | Voltage sensor |
| $V_{1,2}$ | Voltage output 1 and 2 of amplifier, respectively |
| $w$ | Lateral displacement |
| $x$ | Location on length element |

## A Euler-Bernoulli beam FE model

The FE-model of this undamped beam element is calculated via the Euler-Bernoulli approach [33]. This approach introduces the analytical strain energy relation as shown in equation 4. The analytical kinetic energy relation can be given as in equation 5 [17, 33].

$$\sum U = U_b = 0.5 \int_{dL} E_b I_b (\frac{\partial^2 w}{\partial x^2})^2 + E_b A_b (\frac{\partial u_b}{\partial x})^2 dx \tag{4}$$

$$\sum T = T_b = 0.5 \int_{dL} \rho_b h_b b (\dot{w}^2 + \dot{u_b}^2) dx \tag{5}$$

The energy relations can be used to find the EOM of the system, this is done via applying equations 4 and 5 in the Lagrange equation, equation 6.

$$\frac{d}{dt}\frac{\partial \sum T}{\partial \dot{x}} - \frac{\partial \sum T}{\partial x} + \frac{\partial \sum U}{\partial x} = 0 \tag{6}$$

The next step is to define unknown weighting functions $w^h, u_b^h, u_c^h$ and $u_v^h$, to multiply the whole EOM with. $u_c^h$ and $u_v^h$ are not of significance for the bare/undamped beam, however those variables are needed when damping is added to the structure. On this new equation, with weighting functions, partial integration is applied, to reduce the orders of the derivatives. Consecutively the Galerkin method is applied, to find an approximation for the solution of the partial differential equations [22].
Now the EOM can be transformed to FE notation, via defining hermitian shape functions [20], equations 7 and 8. In those equations superscripts give the derivatives, ie. $N^{,xx}$ is the second derivative over x.

$$N_w = \left[\frac{2x^3-3x^2dL+dL^3}{dL^3} \quad \frac{x^3dL-2x^2dL^2+xdL^3}{dL^3} \quad 0 \quad 0 \quad \frac{-2x^3+3x^2dL}{dL^3} \quad \frac{x^3dL-x^2dL^2}{dL^3} \quad 0 \quad 0\right] \tag{7}$$

$$N_b = \begin{bmatrix}0 & 0 & 0 & 1-x & 0 & 0 & 0 & x\end{bmatrix} \tag{8}$$

Applying those shape functions leads to the EOM for a beam element of length dL as shown in equation 9. In which $\overline{u}$ is represented by equation 10.

$$M_b\ddot{\overline{u}} + K_b\overline{u} = F \tag{9}$$

$$\overline{u} = \begin{bmatrix}w & \frac{\partial w}{\partial x} & u_c & u_b\end{bmatrix} \tag{10}$$

$$M_b = \int_{dL} N_w^T \rho_b h_b b N_w + N_b^T \rho_b h_b b N_b dx \tag{11}$$

$$K_b = \int_{dL} N_w^{,xx^T} E_b I_b N_w^{,xx} + N_b^{,x^T} E_b h_b b N_b^{,x} dx \tag{12}$$

## B Piezo beam FE-model

The mass and stiffness matrices of the piezo element and the beam are deviated in a similar manner, as described in detail in appendix A. In this case the strain energy and kintetic energy equations are given in equations 13 and 15.

$$\sum U = U_b + U_p \tag{13}$$

$$U_p = 0.5 \int_{dL} E_p I_p (\frac{\partial^2 w}{\partial x^2})^2 + E_p A_p (\frac{\partial u_p}{\partial x})^2 dx \tag{14}$$

$$\sum T = T_b + T_p \tag{15}$$

$$T_p = 0.5 \int_{dL} \rho_p h_p b_p (\dot{w}^2 + \dot{u_p}^2) dx \tag{16}$$

This leads to mass and stiffness matrices as given in equations 18 and 20, which formulate the EOM of equation 17. In these equations the shapefunction $N_p$ is given by equation 22. This equation is deviated from

Fabbrocino et al. [13], however a small adjustment is made in order to take the thin glue layer in between the piezo transducer and the beam into account.

$$M_{piezo}\ddot{\overline{u}} + K_{piezo}\overline{u} = F \tag{17}$$

$$M_{piezo} = M_b + M_p \tag{18}$$

$$M_p = \int_{dL} N_w^T \rho_p h_p b_p N_w + N_p^T \rho_p h_p b_p N_p dx \tag{19}$$

$$K_{piezo} = K_b + K_p \tag{20}$$

$$K_p = \int_{dL} N_w^{,xx^T} E_p I_p N_w^{,xx} + N_p^{,x^T} E_p h_p b_p N_p^{,x} dx \tag{21}$$

$$N_p = N_b - \frac{h_g(h_b + h_p)}{2} N_w^{,x} \tag{22}$$

## C CLD beam FE model

The strain energy definitions for a CLD covered Euler-Bernoulli beam can be obtained via the Markus and mead approach [23], this approach is an expansions of the Euler-bernoullli method. The stress relations obtained with this method can be transformed into energy equations. This leads to the strain energy equations as given by Huang et al. [17], equations 23 and 24.

$$U_c = 0.5 \int_{dL} E_c I_c (\frac{\partial^2 w}{\partial x^2})^2 + E_c A_c (\frac{\partial u_c}{\partial x})^2 dx \tag{23}$$

$$U_v = 0.5 \int_{dL} G_v A_v (\frac{h_v + 0.5(h_b + h_c)}{h_v} \frac{\partial w(x)}{\partial x} + \frac{u_c - u_b}{h_v})^2 dx \tag{24}$$

In which $U_v$ is simplified to.

$$U_v = 0.5 \int_{dL} G_v A_v \gamma^2 dx \tag{25}$$

$$\sum U = U_b + U_c + U_v \tag{26}$$

The kinetic energy formulations are given by the following equations [17].

$$T_c = 0.5 \int_{dL} \rho_c h_c b_c (\dot{w}^2 + \dot{u_c}^2) dx \tag{27}$$

$$T_v = 0.5 \int_{dL} \rho_v h_v b_c (\dot{w}^2 + \dot{u_v}^2) dx \tag{28}$$

$$\sum T = T_b + T_c + T_v \tag{29}$$

Those energy expressions can be put in the Lagrange equation, in order to find the EOM of the system, equation 6. Further, the method is similar to the method as used for the undamped beam, appendix A. Consequently the EOM is as given in equation 30.

$$M_{CLD}\ddot{\overline{u}} + K_{CLD}\overline{u} = F \tag{30}$$

$$M_{CLD} = M_b + M_c + M_v \tag{31}$$

$$M_c = \int_{dL} N_w^T \rho_c h_c b_c N_w + N_c^T \rho_c h_c b_c N_c dx \tag{32}$$

$$M_v = \int_{dL} N_w^T \rho_v h_v b_v N_w + N_v^T \rho_v h_v b_c N_v dx \tag{33}$$

$$K_{CLD} = K_b + K_c + K_v \tag{34}$$

$$K_c = \int_{dL} N_w^{;xx^T} E_c I_c N_w^{;xx} + N_c^{;x^T} E_c h_c b_c N_c^{;x} dx \tag{35}$$

$$K_v = \int_{dL} N_w^{;xx^T} E_v I_v N_w^{;xx} + N_\gamma G_v h_v b_c N_\gamma dx \tag{36}$$

The shapefunctions are given in equations 37-39. Those shapefunctions consider, among others, the axial displacement difference between the constraining layer and the beam ($u_b$ and $u_c$), this difference defines the shear strain in the viscoelastic layer.

$$N_c = \begin{bmatrix} 0 & 0 & 1-x & 0 & 0 & 0 & x & 0 \end{bmatrix} \tag{37}$$

$$N_v = 0.5(N_c + N_b) + \frac{h_c - h_b}{4} N_w^{;x} \tag{38}$$

$$N_\gamma = \frac{N_c - N_b}{h_v} + \frac{h_v + 0.5(h_b + h_c)}{h_v} N_w^{;x} \tag{39}$$

## D Constructing a beam out of elements

The FE model of each type of element leads to a mass matrix ($M_{element}$) and a stiffness matrix ($K_{element}$) for each element. Those elements need to be connected, by coupling the DOF's of the nodes. This is done via dynamic sub-structuring [10]. An example for the $M_{system}$-matrix, with 2 elements, is given in equation 41. Here $M_{node}^j$ represent the DOFs of node j, in which node j is part of $M_{element}^i$, as shown in equation 40. The same steps are used for the K-matrix.

$$M_{element}^i = \begin{bmatrix} M_{node}^{2i-1} & 0 \\ 0 & M_{node}^{2i} \end{bmatrix} \tag{40}$$

$$M_{system} = \begin{bmatrix} 1 & 0 & 0 & 0 \\ 0 & 1 & 1 & 0 \\ 0 & 0 & 0 & 1 \end{bmatrix} \begin{bmatrix} M_{node}^1 & 0 & 0 & 0 \\ 0 & M_{node}^2 & 0 & 0 \\ 0 & 0 & M_{node}^3 & 0 \\ 0 & 0 & 0 & M_{node}^4 \end{bmatrix} \begin{bmatrix} 1 & 0 & 0 \\ 0 & 1 & 0 \\ 0 & 1 & 0 \\ 0 & 0 & 1 \end{bmatrix} \tag{41}$$

The next step is to implement the boundary conditions, this means for the cantilever beam example all DOF of the first node are set to zero. As shown in equation 42.

$$\overline{u} = \begin{bmatrix} 0 & 0 & 0 & 0 \end{bmatrix} \tag{42}$$

Now the FE-model of the cantilever beam is obtained.

## E Active piezo actuator FE model

The transfer function for the actuator can be found easily, through combining equations 43, 44 and 45. This leads to an actuator force ($F_{act}$) as function of voltage ($V_{act}$) as given in equation 46 [20].

$$\sigma_{piezo} = \frac{\epsilon_{piezo}}{S_{11}^e} - \frac{d_{31} E_{elec}}{S_{11}^e} \tag{43}$$

$$E_{elec} = \frac{V_{act}}{h_p} \tag{44}$$

$$F = \iint_A \sigma dA \tag{45}$$

$$F_{act} = \frac{d_{31} b_p}{S_{11}^e} V_{act} \tag{46}$$

In order to insert this equation into the Lagrange equation, equation 6, it is needed to calculate the virtual work done by this force. This can be done according to equation 47.
The next step is to write this virtual work equation into FE-formulation, via the same method as described in appendix A. The shape function used for the active piezo-element is shown in equation 48. This shape function shows the influence an active element has on the normal strain and the moment in the structure.
All together, this leads to the transfer function as shown in equation 49.

$$\delta W_{act} = \int_{dL} F_{act} \frac{\partial u_p}{\partial x} dx \tag{47}$$

$$N_{p_a} = N_b - \frac{h_g (h_b + h_p)}{2} N_w^{,x} \tag{48}$$

$$\frac{F_{act}}{V_{act}} = \int_d L \frac{d_{31} b_p}{S_{11}^e} N_{p_a}^{,x^T} dx \tag{49}$$

## F Active piezo sensor FE model

The voltage generated in the sensor is dependent on the deformations of the transducer. This makes the sensor equation different from the actuator equation. For the sensor the method from Lee [21] is used, which is applied by Baz et all [6]. This method states that the electrical energy in the piezo transducer needs to be the same as the mechanical energy, this comparison is done through the piezo electric coupling factor ($k_{13}$), as shown in equation 50. Rewriting this equation leads to equation 52. This equation does need to be writen in FE-formulation, and this can be done in the same manner as done for the piezo actuator, as in appendix E. This leads to the finite element formulation as shown in equation 53.

$$\iint_A \frac{1}{2} C_{piezo} V_{sensor}^2 dA = k_{13}^2 \iint_A \frac{1}{2} \sigma_{piezo} \delta u_p dA \tag{50}$$

$$\sigma_{piezo} = \frac{V_{sensor}}{g_{31} h_p} \tag{51}$$

$$\frac{V_{sensor}}{L} = \iint_{dA} \frac{k_{31}^2}{g_{31} C_{piezo} h_p} \delta u_p dA \tag{52}$$

$$\frac{V_{sensor}}{\overline{u}_{sensor}} = \int_{dL} \frac{k_{31}^2 b_p}{g_{31} C_{piezo}} N_{p_a}^{;x} dx \tag{53}$$

## G Positive position feedback

Positive position feedback (PPF) is used to actively damp the structure, this controller is chosen because of its ability to be focussed on a certain eigenfrequency and due to the $2^{nd}$ order roll-off [29]. The tf of the controller is given by equation 54. In this transfer function it can be seen the controller adds flexibility to the system at frequencies below the cut-off frequency. And at higher frequencies it adds stiffness, however this addition is small, due to the controllers roll-off [11].
This means that the controller has an influence on the eigenfrequency peaks below its cut-off frequency only, so if multiple single input-single output (SISO) PPF controllers are used in parallel it is needed to tune from the highest to the lowest eigenfrequency respectively [29].

$$H_{controller} = \frac{g\omega_c^2}{-\omega^2 + 2\xi_{damp}\omega_c \omega i + \omega_c^2} \tag{54}$$

## H Closed-loop transfer function AD

To obtain the closed-loop tf for the AD system, it is needed to define the open-loop tf of the beam first. This can be according to equation 55.

$$Y(s) = M_{system} s^2 + K_{system} \tag{55}$$

The tf of the open-loop system needs to be combined with the tf of the actuator, sensor and controller, appendix E-G. This leads to a closed-loop block diagram as shown in figure 4, given in an tf as shown in equation 56.

$$Y_{act}(s) = (I - Y(s)\frac{F_{act}}{V_{act}} H_{controller} \frac{V_{sensor}}{x_{sensor}})^{-1} Y(s) \tag{56}$$

## I Strain energy distribution

The FE-models provide the EOM of the system, equation 55, those EOM give the relation between force, frequency and displacement. When the force and the frequency are known, it is possible to find all nodal displacements. Those displacements can be used to calculate the strain energy per element, adding those will give the strain energy in the whole flexure.
The equations to calculate the strain energy for respectively a constraining layer, viscoelastic layer and beam element are shown in equations 57-59. Here n is the amount of elements used to describe the whole beam. The stiffness matrices $K_c^n$ and $K_v^n$ are $\overline{0}$-matrices (zero-matrices) if element n is not covered with CLD and those are the stiffness matrix when covered with CLD, as shown in equations 60 and 61.

$$U_c^n = \frac{1}{2} \overline{u}^n K_c^n (\overline{u}^n)^T \tag{57}$$

$$U_v^n = \frac{1}{2} \overline{u}^n K_v^n (\overline{u}^n)^T \tag{58}$$

$$U_b^n = \frac{1}{2}\overline{u}^n K_b (\overline{u}^n)^T \tag{59}$$

$$K_v^n = \begin{cases} \overline{0} & \text{if } n = \text{bare beam element} \\ K_v & \text{elseif } n = \text{CLD covered beam element} \end{cases} \tag{60}$$

$$K_c^n = \begin{cases} \overline{0} & \text{if } n = \text{bare beam element} \\ K_c & \text{elseif } n = \text{CLD covered beam element} \end{cases} \tag{61}$$

The displacement vector $\overline{u}$ is complex, since it represents a damped system. Being complex causes the modeshapes to get discontinuous over one period, as concluded from the phase diagram in figure 25.
However, figure 25 does show that in this case, with using small damping patches, taking the absolute value of $\overline{u}$ provides reliable results, in terms of representing the stress distribution over the whole period. Since in this figure it is seen that the float in phase for the modeshape of the damped case is small, consequently the modeshapes can be considered continuous over the whole period, like the undamped modeshape in figure 25.

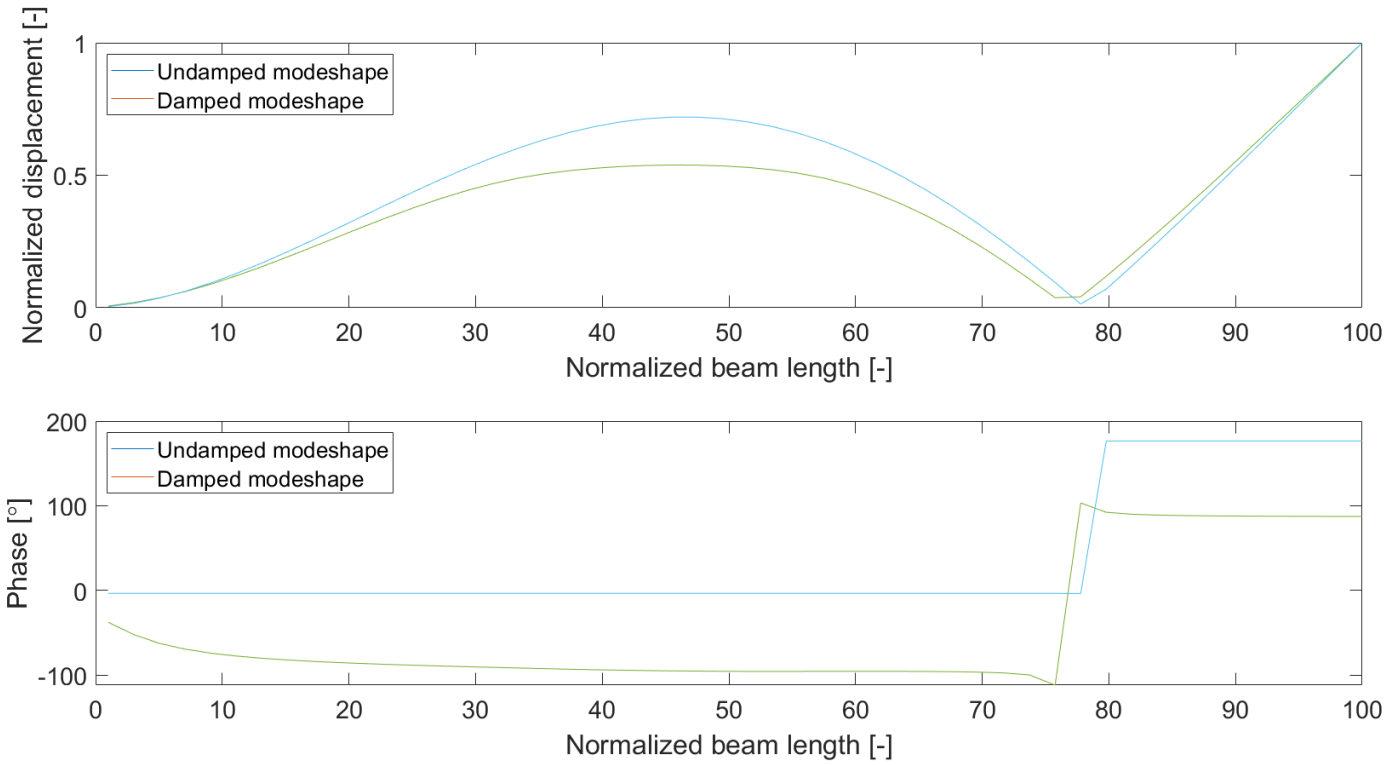


Fig. 25: Comparison modeshape damped and undamped

## J Damping loss factor passive damping

In the preliminaries it is seen the damping loss factor is the ratio of energy dissipated over the total amount of energy stored. This means this value can be calculated in FE-form via equation 62.

$$\eta_{system} = \sum_1^n \frac{U_v^n \eta_v}{U_b^n + U_v^n + U_c^n} \tag{62}$$

## K Energy peak coverage

The definition strain energy peak is given in figure 26. It is defined with this 90% statement, since strain energy peaks are not fully symmetrical and because the slope of the strain energy curve starts to stall at the

boundaries of this statement, figure 26.

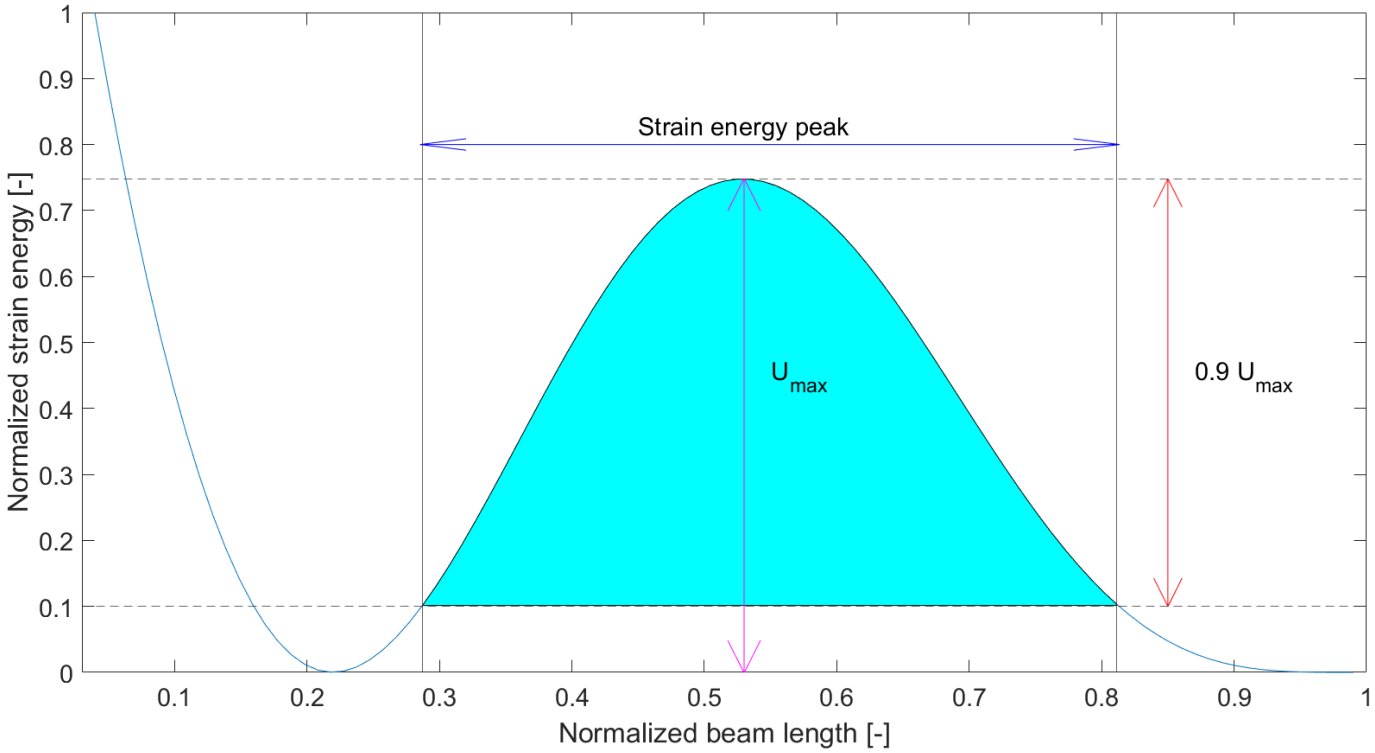


Fig. 26: Visualisation of the definition strain energy peak

## L Tuning the controller

With all system knowledge it is possible to start tuning the PPF. Equation 54 shows it is needed to tune three variables. The first variable to tune is the cut-off frequency, $\omega_c$. Next the gain,g, and the damping factor, $\zeta$, need to be tuned up to optimal performance. This tuning is done for the numerical models as well as the experimental systems. However during tuning it is seen that both give a similar outcome, for g and $\zeta$, when the gain is round-off to an integer and the damping factor to a double with an accuracy of 0.05. $\omega_c$ needs to be tuned for the numerical models and experiments individually, since the locations of the eigenfrequency peaks do slightly differ.
Figure 27 shows the influence different gain and damping factor values have on the frf of the collocated tf from actuator 1 to sensor 1 for the active damping system. Here it is shown that a high gain or a low damping factor will cause a significant local change in the dynamics of the system, in terms of a shift in eigenfrequency peak. This domination of the controller is unwanted, this is the reason that the properties are as shown in table 8.

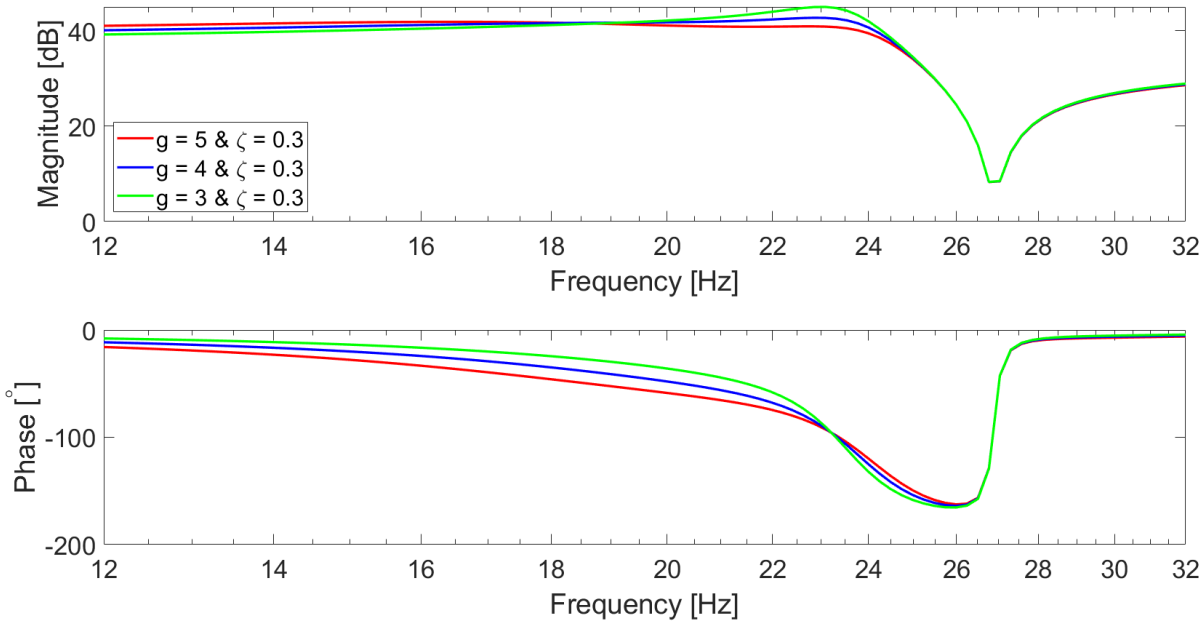


(a) Collocated FRF for damping location 1 for the $1^{st}$ eigenfrequency, varying gain

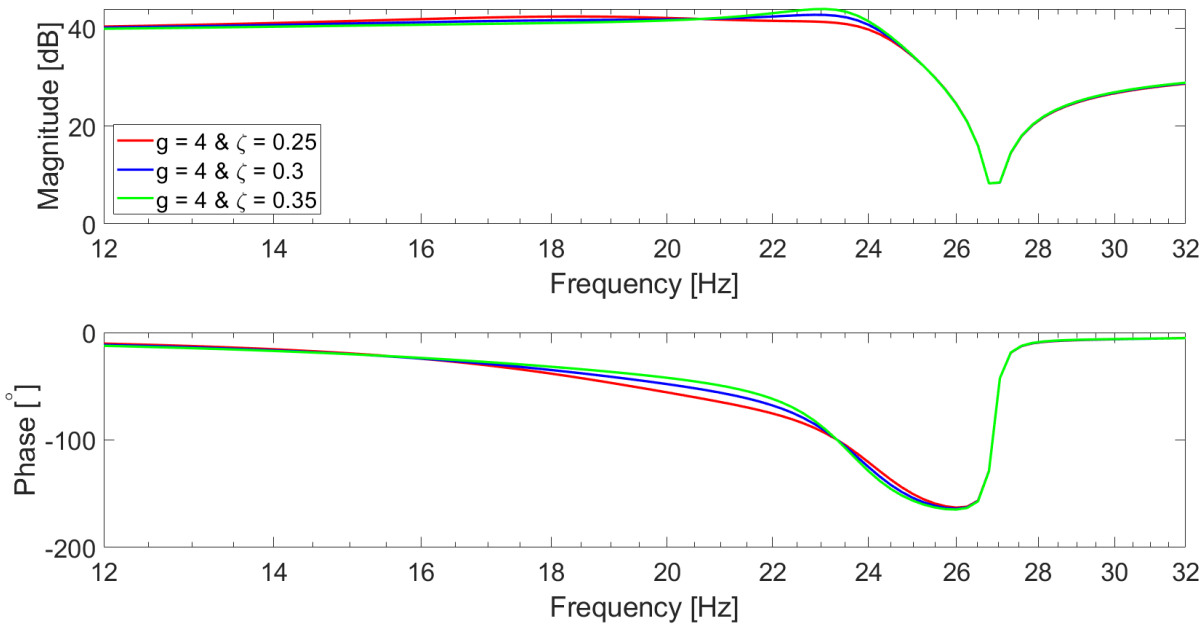


(b) Collocated FRF for damping location 1 for the $1^{st}$ eigenfrequency, varying damping ratio

Fig. 27: Collocated FRF for damping location 1 for the $1^{st}$ eigenfrequency

| | | Active damping | | | Hybrid damping | | |
|---|---|---|---|---|---|---|---|
| | | $\omega_c$ [Hz] | g | $\zeta$ | $\omega_c$ [Hz] | g | $\zeta$ |
| $1^{st}$ eigenfrequency | Numerical | 23.8 | 4 | 0.3 | 24.3 | 4 | 0.3 |
| | Experimental | 24.9 | 4 | 0.3 | 25.7 | 4 | 0.3 |
| $2^{nd}$ eigenfrequency | Numerical | 133.1 | 4 | 0.25 | - | - | - |
| | Experimental | 134.6 | 4 | 0.25 | - | - | - |

Tab. 8: Variables used in PPF

## M Patch dimensions

This appendix does visualize the patch locations, in this visualization does $x_{1x}$ represent the patch designed for the $1^{st}$ eigenfrequency. And $x_{jx}$ represents the patch designed for the $j^{th}$ eigenmode, figure 28. The passive damping system of the experiments exists out of just one patch, since if two patches are used here overlap between the patches would occur.

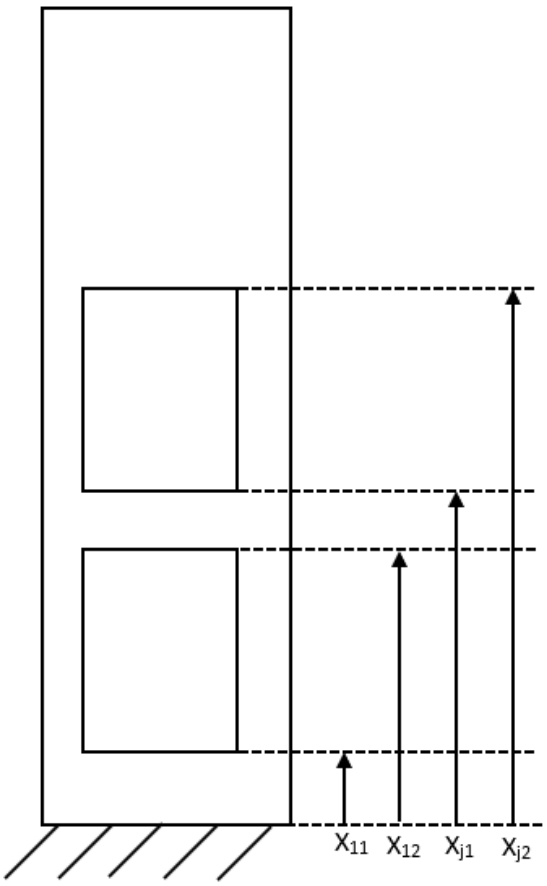


Fig. 28: Schematic visualisation of the described patch locations normalized to the length of the beam, measured from the clamp

| | $x_{11}$ | $x_{12}$ | $x_{21}$ | $x_{22}$ | $x_{31}$ | $x_{32}$ |
|---|---|---|---|---|---|---|
| | Experimental locations | | | | | |
| Active damping | 0.06 | 0.26 | 0.38 | 0.58 | - | - |
| Hybrid damping | 0.06 | 0.26 | 0.28 | 0.72 | - | - |
| Passive damping | 0.06 | 0.92 | - | - | - | - |
| | Optimal locations | | | | | |
| Active damping | 0.06 | 0.26 | 0.38 | 0.58 | 0.60 | 0.80 |
| Passive damping | 0.06 | 0.38 | 0.38 | 0.64 | 0.58 | 0.90 |

Tab. 9: Normalized patch locations for the experimental validation(section 4) and the optimal location (section 3.3)

## N Elaboration of experiments

The elaboration of the experiments is divided into three sections. In the first section the idea behind the set-up itself is elaborated, and how those ideas are implemented. The next section elaborates how this set-up is used to do measurements. The last section will introduce the electrical circuit used for active damping, and the difficulties introduced by this. This section elaborates how all hardware is evaluated. This evaluation is needed to make a reliable comparison between the models and simulations.

### N.1 Motivation behind set-up

The experimental set-up is shown in figure 21, this set-up simulates a cantilever beam with a disturbance actuator as close to the root as possible, which is shown schematically in figure 29. Here the spring re-presents the pre-tension bolt. This bolt is needed since a piezo transducer needs a pre-stress to prevent elongating stresses, which is a weak stress direction of the brittle piezo material [27].
To simulate clamping as good as possible, it is calculated that the stiffness of the clamping is at least 3 times the stiffness of the pre-stress bolt. This is the reason two end-plates are attached at the top of the clamp. Those plates reduce the bending moment in part B, figure 21, thus part B can be considered as infinitely stiff.

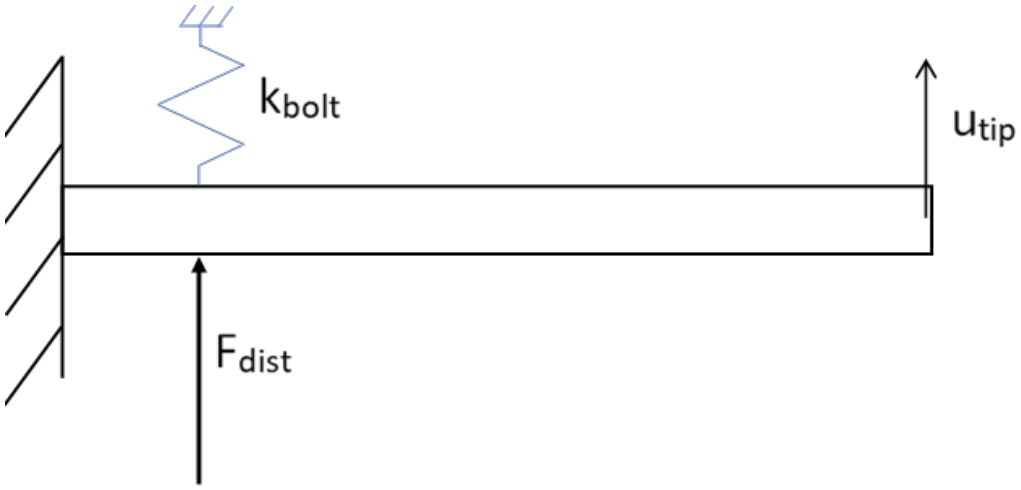


Fig. 29: Schematic visualisation of the experimental set-up

### N.2 Experimental approach

The first step in the experimental approach is to get the set-up on a vibration isolating table, in order to do reliable measurements. Than 2 kinds of sensors are used, a 10mm laser-triangulation sensor, optoNCDT1220-10, for the first measuments [24]. Those first measurements were used to develop a MATLAB-code to calculate the FRF's of the measurements. Those measurements were also used to see if the models and measurements

were roughly the same. Using this sensor led to the conclusion that the set-up was good and that the models were similar to the measurements.
The next step was to implement a more accurate sensor, a single point laser vibrometer, a Polytech OVF-505. This sensor was used to measure the FRF's for all 4 coverage methods, and to compare the experiments with the numerical models. The frf's are developped by exerting a sinusoidal disturbance force with constant amplitude to the beam, the frequency of this force is increased from 1-250Hz. In this frequency region the $1^{st}$ and $2^{nd}$ eigenfrequency can be analyzed. Thus the frf's of the 4 types of beams are researched. The 4 types of beams are shown in figure 30.

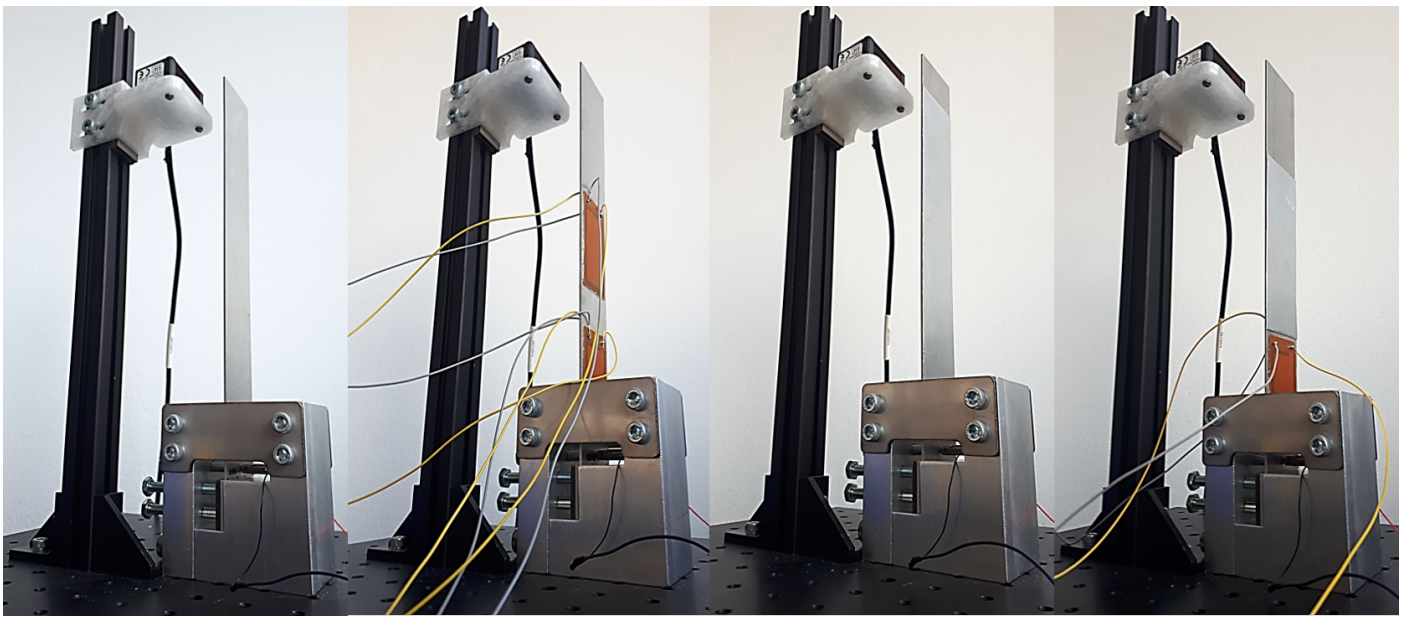

Fig. 30: Pictures of the beam non-covered, full active covered, full passive covered and hybrid covered, respectively

## N.3 Validation active control system

Active damping is implemented as shown in figure 22, in here the x represents a certain location on the beam, as shown with numbers in figure 31.
The visualization of the electronic circuit shows 5 components of the control-loop which can influence performance. Only 3 of those components will be researched thoroughly in section N.3, since the performances of the NI cRIO modules, NI9201 and NI9263, are known. However to use the modules it needs to be noted that the output module is 16-bit and the input modules 12-bit, consequently the gain must be multiplied by a factor $2^4$.

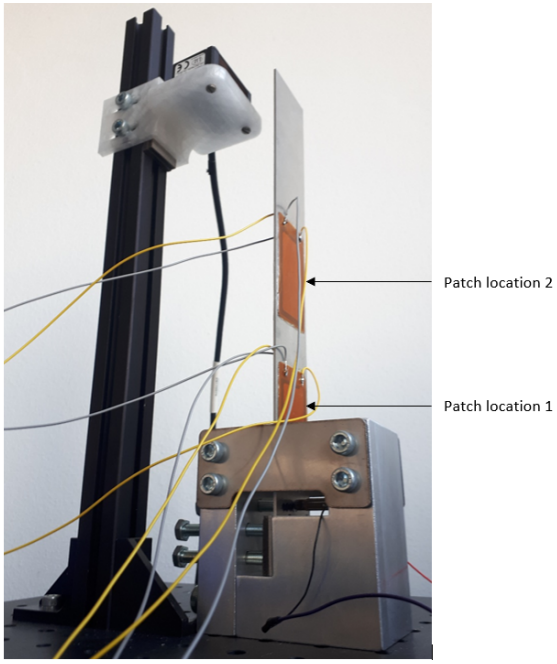


Fig. 31: Visualisation of the experimental set-up with active patches

### N.3.1 Sensor analysis

First, the voltages over the transducers are measured when the beam is actuated at the first eigenfrequency. To see if a sensor and actuator at the same location give a similar voltage, and if those voltages are similar to the numerical models. Table 10 provides an overview of those voltages. In this table it is seen that at location 1 the sensor has a significantly lower efficiency, whereas the actuator and models have similar performances at the other locations. This phenomenon can have different causes, however it is most likely to be caused by bad wiring or changed material properties due to overheating during soldering. To take this voltage difference into account the gain of the controller between sensor 1 and actuator 1 needs to be multiplied by a factor of 1.56, in order to mimic proper performance.
The other voltages are within uncertainty margins, so those do not need a correction in the gain.
Initially the model values did differ more from the experimental values, however the P876-A12 transducers can have a deviation of ±20% on the capacitance[27]. So tuning the capacitance within the margins can lead to a more realistic result, which is done to get to the values as stated in table 10.

| | $1^{st}$ eigenfrequency | | | | | |
|---|---|---|---|---|---|---|
| Damping type | Sensor 1 | Actuator 1 | Model loc.1 | Sensor 2 | Actuator 2 | Model loc.2 |
| Active damping | 6.8V | 10.6V | 9.2V | 3.9V | 3.7V | 3.8V |
| Hybrid damping | 10.7V | 10.8V | 9.6V | - | - | - |

Tab. 10: Comparison of the sensor voltages when the tip displacent has an amplitude of 1mm at the $1^{st}$ eigenmode

### N.3.2 Amplifier analysis

The next step is to analyze the performance of the amplifiers, since the performance of those as function of frequency is unknown. The amplifiers used are the PiezoDrive BD300 amplifiers. Those amplifiers can develop positive voltages only, however by a two-wire configuration a pure sinosiodal wave can be developed in a differential manner. This means two pure positive sinusoidal functions are subtracted from each other, to get a pure sinusoidal output. Consequently those two sinusoids must have the same phase difference at all frequencies, to provide the same output at all frequencies.

Figure 32 shows the time response of the amplifier, when a frequency sweep with constant amplitude is applied. Here it can be seen that the phase difference between $V_1$ and $V_2$ does not vary with frequency. However, the amplification reduces over frequency, which suggest that for example low-pass filtering occurs. The static gain did differ slightly per amplifier, however the experimental static gain is taken into account into the numerical models.
This low-pass filtering limitation as measured is given in a transfer function (tf), as shown in equation 63. A discretized version of the this tf is implemented in the numerical models. The frequency response of the amplifier is given in figure 33.
By implementing the measured limitations into the numerical models it is not needed to have knowledge about the dynamics of the limitations. Nevertheless, this approach enables us to compare the models with the experiments.
The shortcomings of amplifier are an example of electronic hardware limitations limitting active damping performance [29], however it is expected those limitations will not occur at those 'lower' frequencies with better equipment.

$$H_{amp} = \frac{V_1 - V_2}{V_{in}} \tag{63}$$

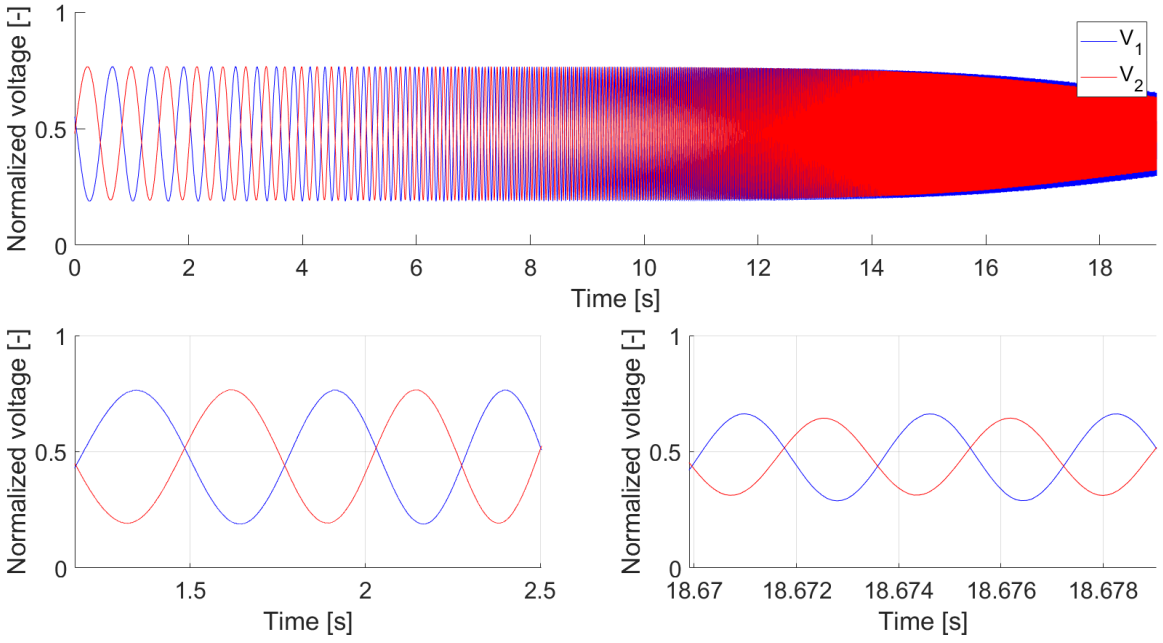


Fig. 32: Amplifier output $V_1$ and $V_2$ as function of time

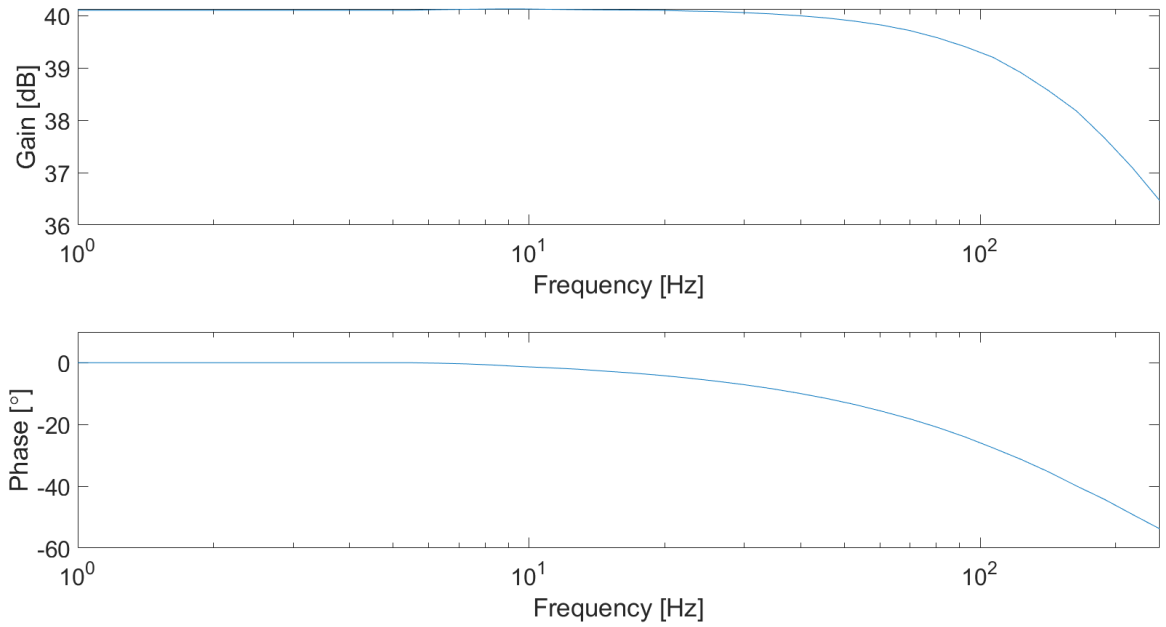


Fig. 33: Frequency response of the amplifier, as given by equation 63

### N.3.3 Actuator analysis

The last step is to analyze actuation performance, this is done by analyzing the beam tip displacement as function of patch voltage. This means each patch is activated individually with a amplitude of 55V at the $1^{st}$ eigenfrequency, and the response beam tip displacement is measured. This results in the beam tip displacements as shown in table 11. In this table it is seen that the tip displacements caused by the actuators are similar for the models and experiments. Although, in the experiments the displacement for the second mode is slightly smaller. This could mean that the patches are not positioned correctly, however the sensor outputs for the $2^{nd}$ eigenfrequency do not have this difference. For this reason it is expected something in the piezo material properties does slightly differ between the models and experiments.

| | $1^{st}$ eigenfrequency | | | | | |
|---|---|---|---|---|---|---|
| Damping type | Sensor 1 | Actuator 1 | Model loc.1 | Sensor 2 | Actuator 2 | Model loc.2 |
| Active damping | 1.1mm | 2.0mm | 2.2mm | 0.67mm | 0.64mm | 0.87mm |
| Hybrid damping | 1.8mm | 2.1mm | 2.1mm | - | - | - |

Tab. 11: Comparison of the tip displacements, when transducers are individually actuated with 55V volt at the $1^{st}$ eigenfrequency